

# Multiple stellar populations in Magellanic Cloud clusters<sup>★,★★</sup>

## I. An ordinary feature for intermediate age globulars in the LMC?

A. P. Milone<sup>1</sup>, L. R. Bedin<sup>2</sup>, G. Piotto<sup>1</sup>, and J. Anderson<sup>2</sup>

<sup>1</sup> Dipartimento di Astronomia, Università di Padova, Vicolo dell'Osservatorio 3, 35122 Padova, Italy  
e-mail: antonino.milone@unipd.it

<sup>2</sup> Space Telescope Science Institute, 3700 San Martin Drive, Baltimore, MD 21218, USA

Received 28 August 2008 / Accepted 14 October 2008

### ABSTRACT

**Context.** The discovery of multiple main sequences (MS) in the massive clusters NGC 2808 and Omega Centauri, along with multiple subgiant branches in NGC 1851 and NGC 6388 has challenged the long-held paradigm that globular clusters consist of simple stellar populations. This evolving picture has been further complicated by recent photometric studies of the Large Magellanic Cloud (LMC) intermediate-age clusters, where the main sequence turn-off (MSTO) was found to be bimodal (NGC 1806 and NGC 1846) or broadened (NGC 1783 and NGC 2173).

**Aims.** We undertook a study of archival HST images of Large and Small Magellanic Cloud clusters with the aim of measuring the frequency of clusters with evidence of multiple or prolonged star formation events and determining their main properties. We found useful images for 53 clusters that cover a wide range of ages. In this paper, we analyse the color-magnitude diagrams (CMD) of sixteen intermediate-age (~1–3 Gyr) LMC clusters.

**Methods.** The data were reduced and the photometry corrected for differential reddening (where required). We find that eleven clusters show an anomalous spread (or split) in colour and magnitude around the MSTO, even though the other main features of the CMD (MS, red giant branch, asymptotic giant branch) are narrow and the horizontal branch (HB) red clump well defined. By using the CMD of the stars in regions that surround the cluster, we demonstrate that the observed feature is unequivocally associated to the clusters. We use artificial-star tests to demonstrate that the spread (or split) is not an artifact due to photometric errors or binaries.

**Results.** We confirm that two clusters (NGC 1806 and NGC 1846) clearly exhibit two distinct MSTOs and observe, for the first time, a double MSTO in NGC 1751. In these three clusters, the population corresponding to the brighter MSTO includes more than two-thirds of the cluster stellar population. We confirm the presence of multiple stellar populations in NGC 1783. Our photometry strongly suggests that the MSTO of this cluster is formed by two distinct branches. In seven clusters (ESO057-SC075, HODGE7, NGC 1852, NGC 1917, NGC 1987, NGC 2108, and NGC 2154), we observed an intrinsic broadening of the MSTO that may suggest that these clusters have experienced a prolonged period of star formation that spans a period between 150 and 250 Myr. The CMDs of IC 2146, NGC 1644, NGC 1652, NGC 1795, and NGC 1978 show no evidence of spread or bimodality within our photometric precision. In summary,  $70 \pm 25\%$  of our sample are not consistent with the simple, single stellar population hypothesis.

**Key words.** galaxies: star clusters – stars: Hertzsprung-Russell (HR) and C-M diagram – Galaxy: globular clusters: general – galaxies: Magellanic Clouds

## 1. Introduction

Nearly all the clusters that have been resolved into individual stars exhibit a colour-magnitude diagram (CMD) consistent with the stars belonging to a single, simple stellar population. In recent years, however, thanks to the improving precision of instruments and techniques (mainly from space), the discovery of multiple populations of stars in stellar clusters is challenging this traditional picture and has led to new views on how clusters form and evolve.

Thus far, photometry has revealed multiple stellar populations in a few Galactic globular clusters (GGCs) i.e. Omega Centauri (Anderson 1997; Bedin et al. 2004; Piotto et al. 2005; Sollima et al. 2007, Villanova et al. 2007), NGC 2808 (D'Antona et al. 2005; Piotto et al. 2007), NGC 1851 (Milone et al. 2008a),

and NGC 6388 (Piotto 2008), also in some intermediate-age Large Magellanic Cloud (LMC) clusters (Bertelli et al. 2003; Mackey & Broby Nielsen 2007 [M07]; Mackey et al. 2008 [M08]) and in the Small Magellanic Cloud (SMC) cluster NGC 419 (Glatt et al. 2008a). Each of the above clusters exhibits a different pattern of age spread and/or chemical enrichment. It is clear that the star-formation history differs from cluster to cluster (see Piotto 2008, for a review).

There is additional photometric evidence that other clusters exhibit some kind of population multiplicity. Marino et al. (2008) find photometric evidence of two distinct stellar populations among the red giant branch (RGB) stars of M4. Yong et al. (2008) find abundance variations in NGC 6752 that correlate with the Strömgren *cy* index and show eight other clusters that present a similar *cy* spread in their giant branches.

In addition, many GGCs, including those with no photometric evidence for multiple populations, exhibit large star-to-star variations in their chemical abundances (see Gratton et al. 2004, for a review). Almost all GGCs have homogeneous

\* Based on observations with the NASA/ESA *Hubble Space Telescope*, obtained at the Space Telescope Science Institute, which is operated by AURA, Inc., under NASA contract NAS 5-26555.

\*\* Table 1, Figs. 13–23, 32–36, 38, and 39 are only available in electronic form at <http://www.aanda.org>

Fe-peak-element abundances (with the only exception being Omega Centauri, hereafter  $\omega$  Cen), but they show a significant dispersion in CNO, Na, Mg, Al, and  $s$ -process elements. The pattern of chemical abundances in GGCs must be primordial as it is observed not only among RGB or asymptotic giant branch (AGB) stars, but also among the sub giant branch (SGB), and most importantly among unevolved stars on the MS (Gratton et al. 2001, 2004). The presence of a well-defined pattern among Na, O, Mg, and Al suggests that most of the GGCs may have hosted multiple episodes of star formation separated by a few hundred Myr (D’Antona & Caloi 2008).

Unfortunately, in an old population, such a difference in age corresponds to a difference of a few hundredths of a magnitude at the level of the MS turn-off (TO) and SGB. At the moment, it is not possible to firmly establish a spread in a cluster’s MSTO with this amplitude, given the presence of differential reddening and difficulties in doing systematically accurate crowded-field photometry at this level of precision.

The families of young and intermediate-age massive clusters that populate the Large and the Small Magellanic Clouds offer us precious opportunities for photometrically searching for multiple stellar populations because, in the CMD of a 1–3 Gyr old cluster, an age interval of 200–300 Myr corresponds to a magnitude difference of a few tenths of a magnitude. Two populations with such a difference could be distinguished easily even at the distance of the Magellanic Clouds (MC).

Indeed, recent photometric studies of LMC clusters have demonstrated that the presence of multiple stellar populations is not a peculiarity of the most massive Galactic GGCs. Bertelli et al. (2003) compare a CMD of NGC 2173 from FORS/VLT data with Padova models and suggest for this LMC cluster a prolonged star-formation episode spanning a period of about 300 Myr. In a recent paper, M08 find that the main-sequence turn off (MSTO) for NGC 1783 reveals a much spread in colour wider than can be explained by photometric errors. Both M07 and M08 also reveal the presence of a double MSTO in the rich intermediate-age clusters NGC 1846 and NGC 1806 of the LMC, and suggest that their CMDs unveil two populations with an age difference of  $\sim 300$  Myr.

Driven by these results on Galactic and LMC clusters, we undertook an analysis of archival HST images of LMC and SMC clusters with the purpose of measuring the frequency of clusters with evidence of multiple or prolonged star formation. The clusters that have been analysed cover a wide range of ages, from  $\sim 10^6$  to  $\sim 10^{10}$  yr. Since the search of multiple populations is carried out through analysis of CMDs, the study of clusters with different ages requires a different sort of analysis.

In this paper, which is the first of a series, we show our entire sample of ACS/WFC CMDs for forty-seven LMC and SMC stellar clusters and present a detailed study of sixteen intermediate-age LMC clusters (between  $\sim 1$  and  $\sim 3$  Gyr). The paper is organised as follow. Section 2 describes the data and the data reduction techniques. In Sect. 3 we present the CMDs of the sixteen intermediate-age clusters. In Sect. 4, we confirm the split of the MSTO of NGC 1806 and NGC 1846 and observe, for the first time, two distinct MSTOs in NGC 1751. We analyse the CMD of these clusters in detail and measure the fraction of stars belonging to each of their MSTO populations. We confirm the presence of multiple stellar populations in NGC 1783 and suggest that the MSTO of this cluster should be formed by two distinct branches. In Sect. 5 we note an anomalous spread around the MSTO of seven clusters: ESO057-SC075, HODGE 7, NGC 1852, NGC 1917, NGC 1987, NGC 2108, and NGC 2154. In Sect. 6 we demonstrate that the observed spread

in the MSTO region of these clusters must be real, since it cannot stem from differential reddening, field contamination, photometric errors, or binary stars. In Sect. 7 we determine the cluster ages and the age differences among different stellar populations in the same cluster through isochrone fitting. Finally, Sect. 8 includes a short summary of our results.

## 2. Observation and data reduction

To investigate the presence of multiple stellar populations in Magellanic Cloud clusters we searched the MAST STScI-archive for HST images collected with the Wide Field Channel (WFC) of the Advanced Camera for Surveys (hereafter ACS/WFC). We found useful images for 53 clusters from GO 9891 (PI: G. F. Gilmore), GO 10395 (PI: J. S. Gallagher) and GO 10595 (PI: P. Goudfrooij). The result of this search is presented in Table 1 for 47 clusters from GO 9891 and GO 10595, while the GO 10396 data set described in Table 1 of Glatt et al. (2008b) (which includes six SMC clusters) will be used in a future paper focused on SMC.

The photometric reduction of the ACS/WFC data was carried out using the software presented and described in detail in Anderson et al. (2008). It consists in a package that analyses all the exposures of each cluster simultaneously to generate a single list of stars for each field. Stars are measured independently in each image by using the best available PSF models from Anderson & King (2006).

This routine was designed to work well in both crowded and uncrowded fields, and it is able to detect almost every star that can be detected by eye. It takes advantage of the many independent dithered pointings of each scene and the knowledge of the PSF to avoid including artifacts in the list. Calibration of ACS photometry into the Vega-mag system was performed following recipes in Bedin et al. (2005) and using the zero points given in Sirianni et al. (2005).

### 2.1. Selection of the star sample

Stars can be poorly measured for several reasons: crowding by nearby neighbours, contamination by cosmic-rays (CRs), or image artifacts such as hot pixels or diffraction spikes. The goal of the present work is to clearly identify multi-populations. For this purpose we need to select the best-measured stars in the field (i.e., those with the lowest random and systematic errors), but we also need to have a large enough statistical sample to be able to identify secondary sequences that may have many fewer members than the primary ones.

The software presented by Anderson et al. (2008) provides very valuable tools for reaching this goal. In addition to the stellar fluxes and positions it provides a number of parameters that can be used as diagnostics of the reliability of photometric measurements. Specifically, these are,

- the rms of the magnitudes measured in different exposures ( $\text{rms}_{m_{F435W}}$ ,  $\text{rms}_{m_{F555W}}$ , and  $\text{rms}_{m_{F814W}}$ , available only for clusters with more than one exposure in the same filter, cf. Table 1);
- the rms of the positions measured in different exposures transformed in a common distortion-free reference frames ( $\text{rms}_x$ , and  $\text{rms}_y$ );
- the residuals to the PSF fit for each star ( $q_{m_{F435W}}$ ,  $q_{m_{F555W}}$ , and  $q_{m_{F814W}}$ ; what Anderson et al. 2008 define as *quality fit*);
- the ratio between the estimated flux of the star in a 0.5 arcsec aperture, and the flux from neighbouring stars within

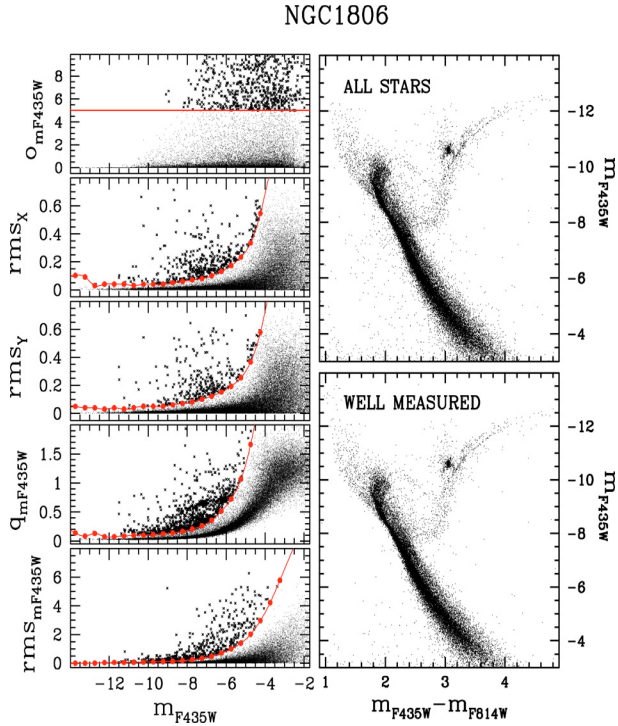


**Fig. 1.** Diagnostic parameters used to select the stars with the best photometry are plotted as a function of  $m_{F435W}$  for NGC 1806. Red lines separate the well-measured stars (thin points) from those that are more likely to have a poorer photometry (thick points). On the right we compare the CMD of all the measured stars (*top*) and of stars that pass our criteria of selection (*bottom*).

the same aperture ( $o_{m_{F435W}}$ ,  $o_{m_{F555W}}$ , and  $o_{m_{F814W}}$ , again see Anderson et al. 2008, for details).

We used these parameters to select a sub sample of stars with the best photometry.

In the five left hand panels of Fig. 1, we show the criteria we used to select the sample of stars with the best photometry in the  $F435W$  band for NGC 1806. The photometric system at this stage is kept in instrumental magnitudes,  $-2.5 \log_{10}(\text{flux})$ , where the flux is expressed in photo-electrons recorded in the reference exposure.

We note a clear trend in the quality-fit and rms parameters as a function of the magnitude due to the decreasing signal-to-noise ratio (S/N). To select well-measured stars at different S/N we adopted the following procedure. We began by dividing all the stars into magnitude bins. The size of each bin varied from one cluster to another depending on the number of stars; for each of them, we computed the median rms ( $q$ ) and the 68.27th percentile (hereafter  $\sigma$ ). The median was derived recursively: after each computation, all stars exceeding four times  $\sigma$  were provisionally rejected until the next iteration and the median was recomputed. This procedure was repeated until two subsequent measures of the median differ by less than the 1% of the value.

Finally, we arrived at the red line of Fig. 1 by adding to the median of each bin  $N$  times  $\sigma$ . This gave us the red circles, which we then fitted with a spline. All stars below the red line in each plot were flagged as well-measured. The factor  $N$  ranges from 5 to 6, and was chosen to draw the boundaries that follow the bulk of the distribution of each parameter value.

The neighbour-contamination parameters do not show a clear trend with magnitude, so we simply flagged all the stars with  $o_{m_{F435W}}$ ,  $o_{m_{F555W}}$ ,  $o_{m_{F814W}} < 5$  as well-measured.

Obviously, the rms of the magnitudes was not available in the case of clusters with only one image per band (HODGE 7, IC 2146, NGC 1644, NGC 1652, NGC 1795, NGC 1852, NGC 1917, NGC 1978, and NGC 2154). In such cases those selections were not applied. In the right panels of Fig. 1 we show the CMD of all the measured stars of NGC 1806 (*top*) and of stars that pass all the selection criteria (*bottom*).

## 2.2. Artificial-star tests

The artificial-star (AS) experiments used in this paper were run following the procedures described in Anderson et al. (2008). First of all, for each cluster, we produced an input list with about  $10^5$  stars located on the entire ACS field of view. It includes the coordinates of the stars ( $X_{in}$ ,  $Y_{in}$ ) in the reference frame, and the magnitudes in the  $F435W$  (or  $F555W$ ) and  $F814W$  bands ( $m_{v_{in}}$ ,  $m_{i_{in}}$ ). We generated the artificial stars with a flat luminosity function in the  $F814W$  band and with instrumental magnitudes from  $-5$  to  $-14$ . We placed artificial stars fainter than the MSTO on the MS ridge line that is determined as described in Sect. 6.2.1 and added artificial stars brighter than the MSTO along the isochrone that fits the observed CMD best (see Sect. 7).

The program described in Anderson et al. (2008) allows artificial-star tests to be performed for one star at a time and entirely in software guaranteeing that artificial stars will never interfere with each other, no matter how many tests are done. Therefore it makes it very simple to do artificial star tests because it is not necessary to add an array of non-interfering stars on the images, reducing all the images each time. For each star in the input list, the routine adds the star to each exposure at the appropriate place with the appropriate flux, and measures the images in the same manner as real stars, producing the same output parameters as in Sect. 2.1. If the input and the output positions differ by less than 0.5 pixel and the fluxes differ by less than 0.75 mag, then the artificial star is considered as found.

Artificial stars played a crucial role in this analysis by allowing us to determine the completeness level of our sample and to measure the fraction of chance-superposition “binaries”. The completeness depends on the crowding conditions, as well as on stellar luminosity. Our procedures account for both of these. Our goal in the AS tests is to probe how incompleteness and photometric errors vary with crowding or brightness. As a result, we generated a list of artificial stars that had colours that placed them on the average cluster sequence and positions drawn from the overall cluster radial distribution.

We divided the ACS/WFC field for each cluster into 5 concentric annuli centred on the cluster centre, and within each annulus we examined the AS results in eight magnitude bins, from  $-14$  to  $-5$ . For each of these  $5 \times 8$  grid points, we then determined the average completeness by taking the ratio of the recovered to input artificial stars within that bin. This grid then allowed us to estimate the completeness for any star at any position within the cluster. As an example, the left panel of Fig. 2 shows the completeness as a function of the instrumental  $m_{F814W}$  magnitude in each of the five annuli used to divide the field of NGC 1806. Finally, we interpolated the grid points and derived the completeness value associated with each star. The right panel of Fig. 2 shows the completeness contours in the radius versus  $m_{F814W}$  magnitude plane. Continuous lines correspond to completeness levels of 0.25, 0.50, and 0.75. Dotted lines indicate differences of completeness of 0.05.

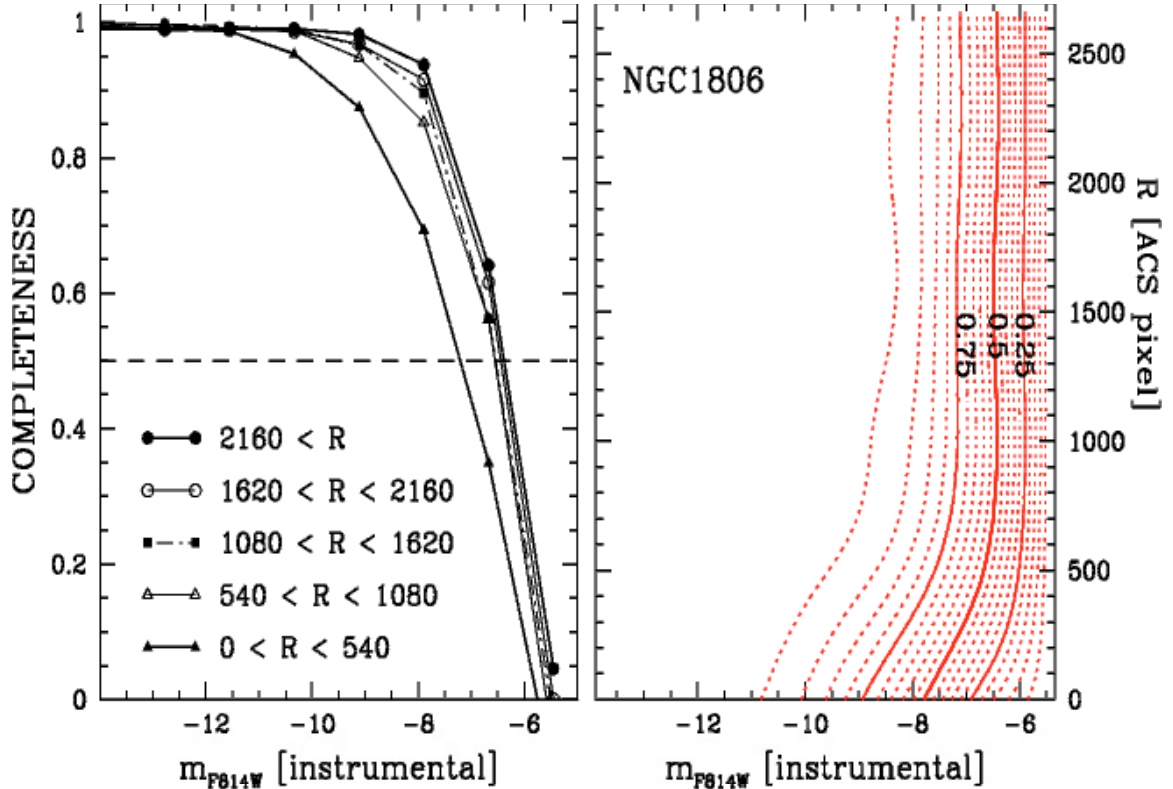


**Fig. 2.** *Left:* completeness as a function of the  $m_{F814W}$  magnitude in five annuli. *Right:* completeness contours in the radial distance versus  $m_{F814W}$  magnitude plane.

### 3. The cluster CMDs

In Fig. 3 we show the instrumental  $m_{F555W}$  versus  $m_{F555W} - m_{F814W}$  CMDs of all the 47 clusters from GO 9891 and GO 10595 presented in Sect. 2. It is clear from this figure that our sample contains clusters at many different stages of evolution. This paper will deal with the CMDs of the sixteen intermediate-age clusters (from  $\sim 1$  to  $\sim 3$  Gyr). The other clusters will be covered in forthcoming papers. All selected intermediate age clusters are LMC members.

Most of the CMDs plotted in Fig. 3 show considerable evidence of contamination, mainly due to MC field stars. For the purposes of this paper, it is crucial to determine the stellar distribution in the field-star CMD as well as possible, since without such attention, field sequences could be erroneously attributed to the cluster and interpreted as an additional population.

Since most of the clusters of our sample cover a small portion of the ACS/WFC field of view, we can easily isolate a CMD that is representative of the field population surrounding the cluster by selecting the portion of the ACS/WFC image that is farthest from the cluster centre, so that the contamination of cluster members should be negligible and, in many cases, almost absent.

To minimize the fraction of field stars in the cluster CMD, we selected two regions with the same area. The first region, which below we call the “cluster field”, is centred on the cluster and includes the region with the highest density of cluster members (with NGC 1978 the only exception, where we chose an annulus around the cluster centre to exclude the crowded cluster core). The second region is far enough from the cluster center that very few cluster stars would be expected to be present there. We will call this field “reference field” and its stars should be representative of the typical population in front of and behind the cluster. Since cluster stars in the vicinity of the MSTO are the main

targets of the present study, we defined the area of these regions such that the density of stars within a magnitude from the TO, namely with  $m_{F814W} < (m_{F814W}^{TO} + 1)$ , in the cluster field would be at least a fixed number ( $N$ ) of times that of the reference field. In most cases we could set  $N = 5$ , which would mean that, even without field correction, we have at most a 20% contamination. An exception is NGC 1917, which is projected upon a densely populated region of the LMC. In this case we used  $N = 3$ . For the most populated clusters (IC 2146, NGC 1806, NGC 1846, and NGC 1978), we adopted  $N = 10$ .

In Fig. 4, we compare the CMDs of the cluster and reference fields for the sixteen intermediate age clusters that have been studied in this paper. All the reference-field CMDs selected with this criterion share a broadened, young main sequence and a 5–6 Gyr old stellar population that departs from the MS at around  $m_{F555W} = 22.5$  and populates the evolved portions of the CMD. In Sect. 6.1 we use the CMDs of the reference field to decontaminate the CMD of the cluster.

#### 3.1. Differential reddening

It is well known that differential reddening causes a shift in all the CMD features parallel to the reddening line and tends to randomly broaden them. A quick look at the CMDs presented in this paper shows that most of the RGBs and AGBs are narrow and well defined, and that the HB red clump is compact. Moreover, we have divided the cluster field into many subregions (the exact number varies from one cluster to another, depending on the number of stars) and compared the CMDs of stars located in each of them. In most cases, we found no evidence of any offset among the CMDs, and so, any variations in reddening should be negligible.

## WFC/ACS observations

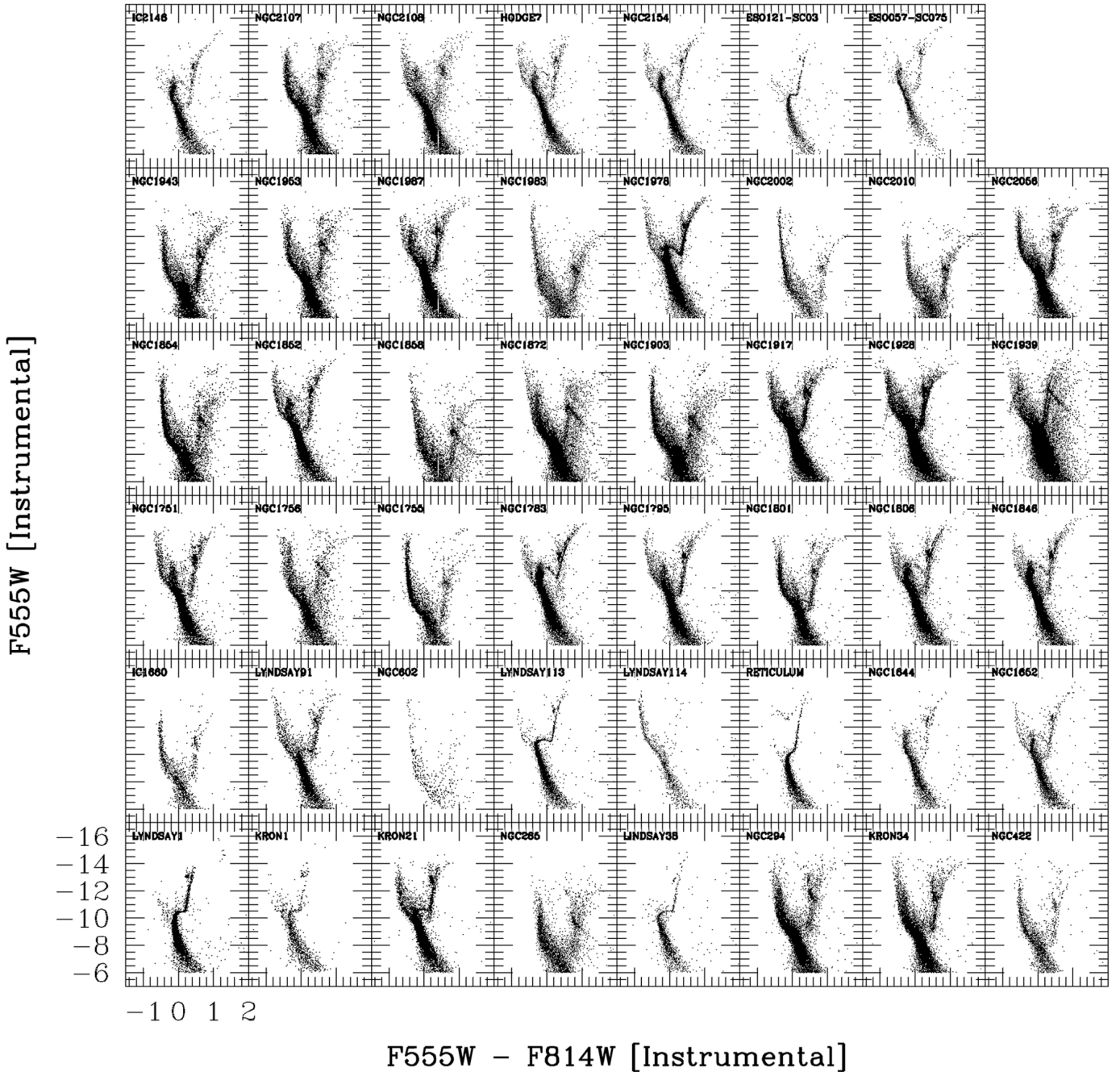


Fig. 3. Instrumental  $m_{F555W}$  vs.  $m_{F555W} - m_{F814W}$  for 47 MCs clusters.

Two exceptions to this reddening-free rule are NGC 1751 and NGC 2108. We show their CMD in Figs. 5 and 6. The confused shape of the HB red clumps and of other primary features suggests differential reddening. Since differential reddening acts along the direction of the reddening arrow shown at the lower left, sequences (such as the SGB) that are aligned perpendicular to the reddening line are most affected.

For this reason, a search for a possible split or a spread around the MSTO requires an accurate correction of the effects produced by differential reddening on the observed CMD. To correct for differential reddening, we used the procedure described in Sarajedini et al. (2007). Briefly, we define the fiducial main sequence for the cluster and tabulate, with a grid of points across the field, how the observed stars in the vicinity of each

grid point may systematically lie to the red or the blue of the fiducial sequence; this systematic colour offset is indicative of the local differential reddening.

In the lower panel of Fig. 5, we show the corrected CMD of NGC 1751. It should be noted how, after the correction has been applied, all the main features of the CMD become narrower and clearly defined, confirming that most of the effects of differential reddening have been removed. The improvement of the CMD is particularly evident for the stars of the HB red clump; the tightness along the reddening line of this clump means that the spread (or split) we see in the MSTO cannot be due to differential reddening. Figure 6 illustrates the effects of the reddening correction in NGC 2108. The total amount of differential reddening

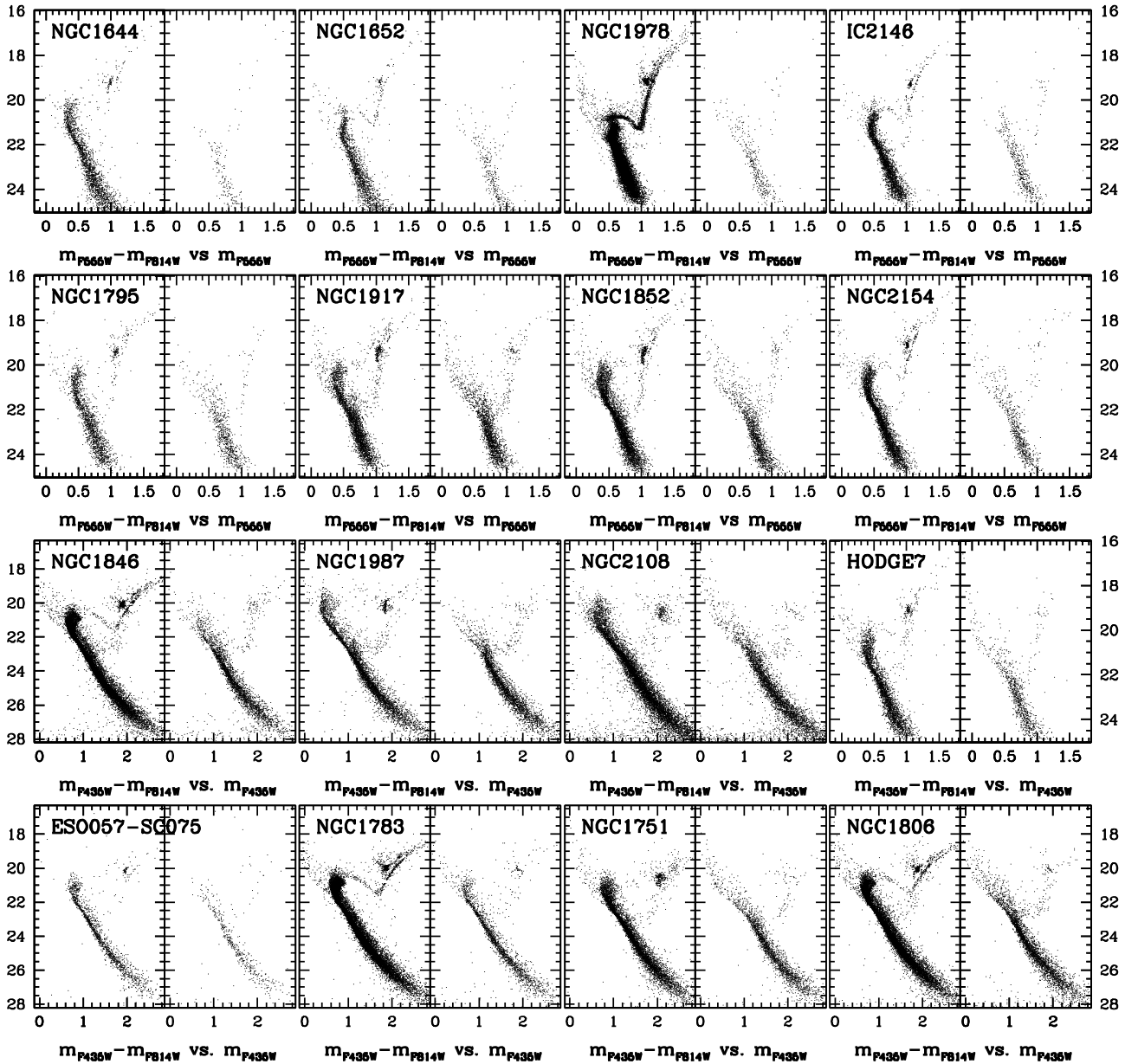


Fig. 4. Comparison of the CMD of cluster and reference fields for the 16 selected intermediate-age clusters.

within the cluster region is  $\Delta E(F435W - F814W) = 0.10$  for NGC 1751 and  $\Delta E(F435W - F814W) = 0.08$  for NGC 2108.

The two clusters that suffer from sizable differential reddening are not at any particular angular distance from the centre of the LMC or with respect to the Milky Way, compared to the other fourteen clusters. They might just fall in some poorly known gas-dust complex structure, and/or with a limited spatial extension.

#### 4. Clusters with a double MSTO: NGC 1806, NGC 1846, and NGC 1751

At least three clusters of our sample clearly show two distinct MSTOs: NGC 1846, NGC 1806, and NGC 1751. The split is evident in the CMDs of the cluster fields that are shown in Figs. 7–9, and is exalted by the Hess diagram in the inset. The presence of two, distinct TOs in NGC 1806 and NGC 1846 was discovered by M07 and M08, who also found no difference in the spatial distribution between the stars in the brighter and fainter MSTOs

(hereafter *b*MSTO and *f*MSTO). In this work, we take advantage of the high photometric quality of our CMDs to measure the fraction of stars belonging to each turnoff population. To do this, it is necessary to select and compare the two groups of *b*MSTO and *f*MSTO.

This procedure is illustrated in Fig. 10 for NGC 1806. We used the CMD of the cluster field, with foreground/background contamination removed as described in Sect. 6.1. We began by finding the isochrones that went through the two sequences and the giant branch (as will be described in detail in Sect. 7). These are the red and blue lines. We then defined by hand two pairs of reference points:  $P_{1,f}$  and  $P_{2,f}$  on the *f*MSTO isochrone and  $P_{1,b}$  and  $P_{2,b}$  on the *b*MSTO isochrone. The two pairs of points were chosen with the criterion of delimiting the region of the CMD where the split is more evident and were used to draw the grey lines in panel (a). Only stars contained in the region between these lines have been used for the following analysis.

In panel (b), we shifted and rotated the reference frame such that the new origin corresponds to  $P_{1,f}$  and the abscissa goes

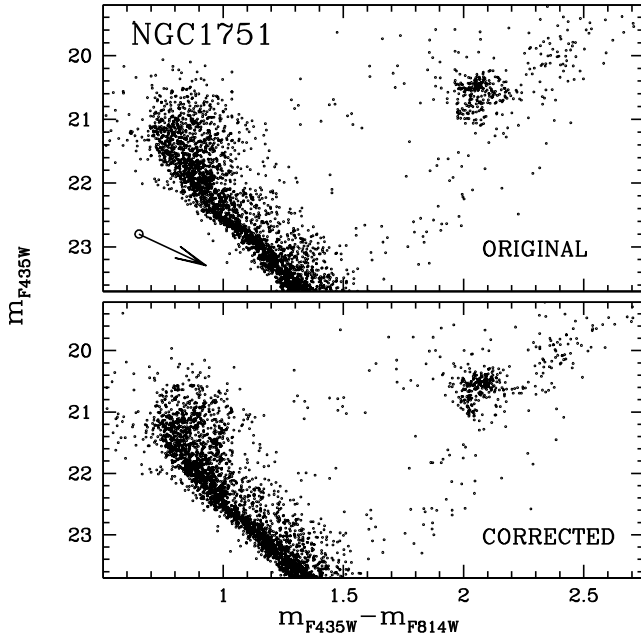


**Fig. 5.** Comparison between the CMD of NGC 1751 before (*top panel*) and after (*bottom panel*) the correction for differential reddening. The arrow indicates the reddening direction.

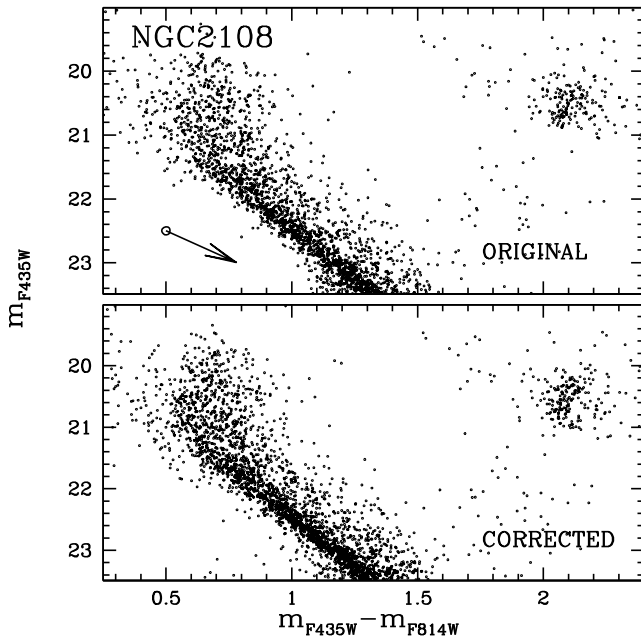


**Fig. 6.** As in Fig. 5 for NGC 2108.

from  $P_{1,b}$  to  $P_{1,f}$ . For simplicity, in the following, we refer to the abscissa and ordinate of this reference frame as “colour” and “magnitude”. The red dashed line is a fiducial line through the region close to the  $f$ MSTO. We drew it by marking four points on the region close to the  $f$ MSTO, equally spaced in “magnitude” and drawing a line through them by means of a spline fit.

In panel (c) the “colour” of this line was subtracted from the colour of each star, and the “magnitude” of each star has been divided by the “magnitude” of a stars with the same “colour” that lies on the line that goes from  $P_{2,f}$  to  $P_{2,b}$ .

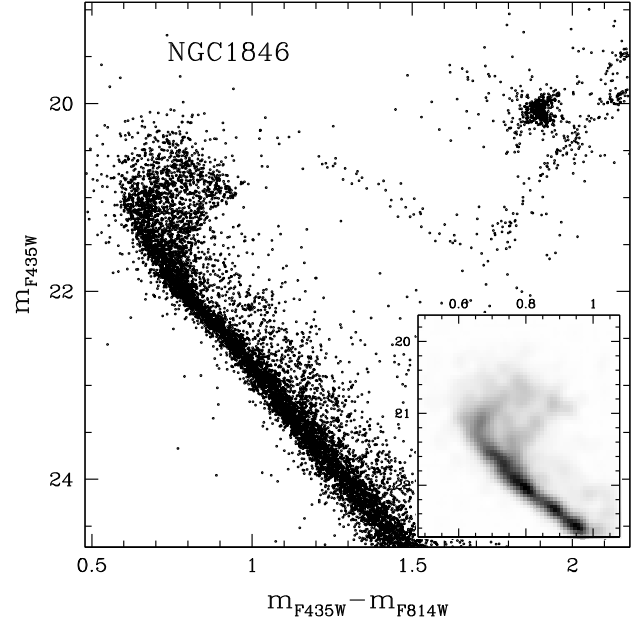


**Fig. 7.** CMD of NGC 1846. All detected sources in the inner field that successfully passed all the selection criteria have been plotted. In the inset we show the Hess diagram for the CMD region around the MSTO.

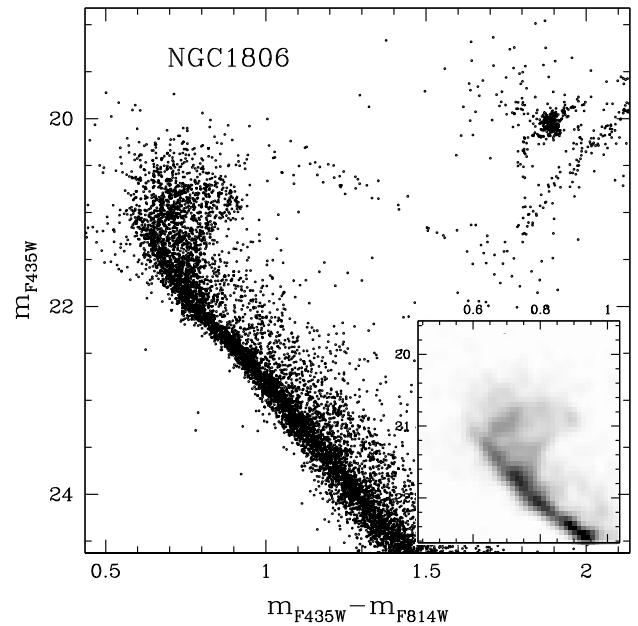


**Fig. 8.** As in Fig. 7 for NGC 1806.

For the analysis that follows, we have divided the  $\Delta$  “magnitude” range into  $N$  bins. We used  $N = 4$  for NGC 1806 and NGC 1846 and  $N = 2$  for the less populated NGC 1751. In each of them, we determined the fraction of stars belonging to each MSTO as follows. Our aim was to model the  $\Delta$  “colour” distribution by fitting the sum of two partially overlapping Gaussians, but we need to reduce the influence of outliers (such as stars with poor photometry, residual field stars, and binaries). To this end, we did a preliminary fit of the Gaussians using all available stars, then we rejected all the stars more than two  $\sigma_b$  distant and less than  $2 \sigma_f$  from the  $f$ MSTO and repeated the fit (where the  $\sigma$ ’s

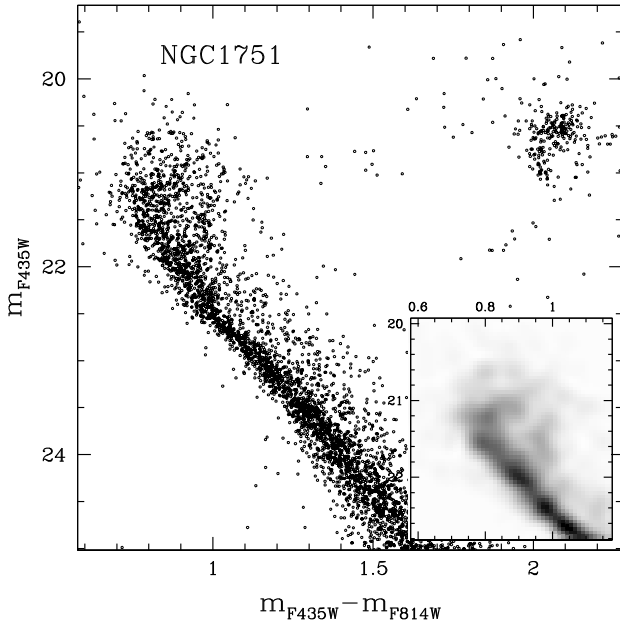


Fig. 9. As in Fig. 7 for NGC 1751.

are those of the best fitting Gaussians in each  $\Delta$  “magnitude” bin fitted to the  $f$ MSTO and  $b$ MSTO respectively).

The continuous vertical lines show the centres of the best-fitting Gaussians in each  $\Delta$  “magnitude” interval. The red dashed line is located two  $\sigma_f$  on the “blue” side of the  $f$ MSTO and the blue line runs two  $\sigma_b$  on the “red” side of the  $b$ MSTO.

It is important to notice here that, to each point ( $P_{1,f(b)}$ ,  $P_{2,f(b)}$ ) that we have arbitrarily selected on the two isochrones with the only purpose to disentangle the two SGBs, corresponds to a mass ( $M_{P_{1,f(b)}}$ ,  $M_{P_{2,f(b)}}$ ). To obtain a more correct measure of the fraction of stars in each of the two populations ( $f_{b\text{MSTO}}$ ,  $f_{f\text{MSTO}}$ ) it must be noted that we are dealing with two different mass intervals ( $M_{P_{2f}} - M_{P_{1f}} \neq M_{P_{2b}} - M_{P_{1b}}$ ) and we have to compensate for two facts: first, more massive stars are rarer, and second, more massive stars evolve faster.

We calculated the fraction of stars in each branch as,

$$f_{b\text{MSTO}} = \frac{\frac{A_b}{N_b/N_f}}{A_f + \frac{A_b}{N_b/N_f}}$$

$$f_{f\text{MSTO}} = \frac{A_f}{A_f + \frac{A_b}{N_b/N_f}}$$

where  $A_b$  and  $A_f$  are the area of the Gaussians that best fit the  $b$ MSTO and the  $f$ MSTO, and  $N_{f(b)} = \int_{P_{1,f(b)}}^{P_{2,f(b)}} \phi(M) dM$ , being adopting for  $\phi(M)$  the Salpeter (1955) IMF.

We find that  $74 \pm 4\%$  of stars of NGC 1806 belong to the  $b$ MSTO and  $26 \pm 4\%$  to the  $f$ MSTO. In the case of NGC 1846, we have  $75 \pm 3\%$  of stars in the  $b$ MSTO and  $25 \pm 3\%$  in the  $f$ MSTO. Finally,  $69 \pm 4\%$  of the NGC 1751 stars belong to the  $b$ MSTO and the  $31 \pm 4\%$  to the  $f$ MSTO. Interestingly enough, a similar population ratio between the bright and the faint SGB ratios has been found in the Galactic globular clusters NGC 1851 (Milone et al. 2008a) and NGC 6388 (Piotto et al., in preparation). We note here that D’Antona & Coloi (2008) predict that more than 50% of the cluster stars must be coming from the second (younger) population in their intermediate mass AGB ejecta pollution scenario proposed to explain multiple populations in star clusters.

#### 4.1. The (double?) MSTO of NGC 1783

A spread in colour around the MSTO of NGC 1783 was first noted by Mucciarelli et al. (2007). Unfortunately their  $m_{F555W}$  versus  $m_{F555W} - m_{F814W}$  CMD had low photometric accuracy, because it was obtained from the GO 9891 images alone. Therefore, they were unable to distinguish between the intrinsic spread in colour and the broadening expected by photometric uncertainties. M08 obtained a CMD for this cluster from data with higher S/N (using both GO 10595 and GO 9891 images) and demonstrated that NGC 1783 shows a much wider spread in colour than what would be expected by photometric errors alone.

Our CMD of NGC 1783 is shown in Fig. 11 and clearly confirms the anomalous spread around the MSTO. In addition, the Hess diagram in the inset reveals a split MSTO and strongly suggests that the apparent spread could be attributed to two distinct branches that are closely spaced and poorly resolved by the observations.

### 5. Possible evidence of prolonged star formation

The CMDs around the MSTO loci for the remaining twelve intermediate-age clusters that have been studied in this work are presented in Figs. 12–23. Unfortunately, being this an archive project, the photometric data set available for these twelve clusters is not homogeneous. One short and two deep images for each of the three filters:  $F435W$ ,  $F555W$ , and  $F814W$ , were collected within program GO 10595, while one single deep image in both  $F555W$  and  $F814W$  bands were collected within the snap-shot program GO 9891. Only two clusters were observed by both programs (NGC 1987 and NGC 2108), one cluster (ESO057-SC075) only in GO-10595, and the remaining nine (HODGE 7, IC 2146, NGC 1644, NGC 1652, NGC 1795, NGC 1852, NGC 1917, NGC 1978, and NGC 2154) were observed within GO 9891 only (see Table 1 for more details).

We find that seven of these clusters show hints of an intrinsic spread around the MSTO: ESO057-SC075, HODGE 7, NGC 1852, NGC 1917, NGC 1987, NGC 2108, and NGC 2154. The CMDs of IC 2146, NGC 1644, NGC 1652, NGC 1795, and NGC 1978 show no evidence of such a spread and are all consistent with hosting stars with the same age and chemical composition, within our photometric precisions. When simulated CMDs are introduced, we will give a more objective criterion for distinguishing clusters with an intrinsic spread around the MSTO (at the end of Sect. 6.2.2).

It must be noted that, apart from the broadened MSTO region, the other primary features of the CMDs of these clusters (MS, RGB, and AGB) are narrow, and the HB red-clump is well-defined, thus the spread cannot be an artifact produced by differential reddening or variations in photometric zero points along the ACS field.

The limited statistic and photometric resolution do not allow us to establish whether these spreads are just unresolved splits-like those identified in the more populous clusters described in Sect. 4- or not.

In the following section, we show that the spread around the MSTO of the clusters mentioned above must be intrinsic. To do this, we demonstrate that the broadening we see cannot be explained by any combination of photometric errors, field-star contamination, or unresolved photometric binaries.

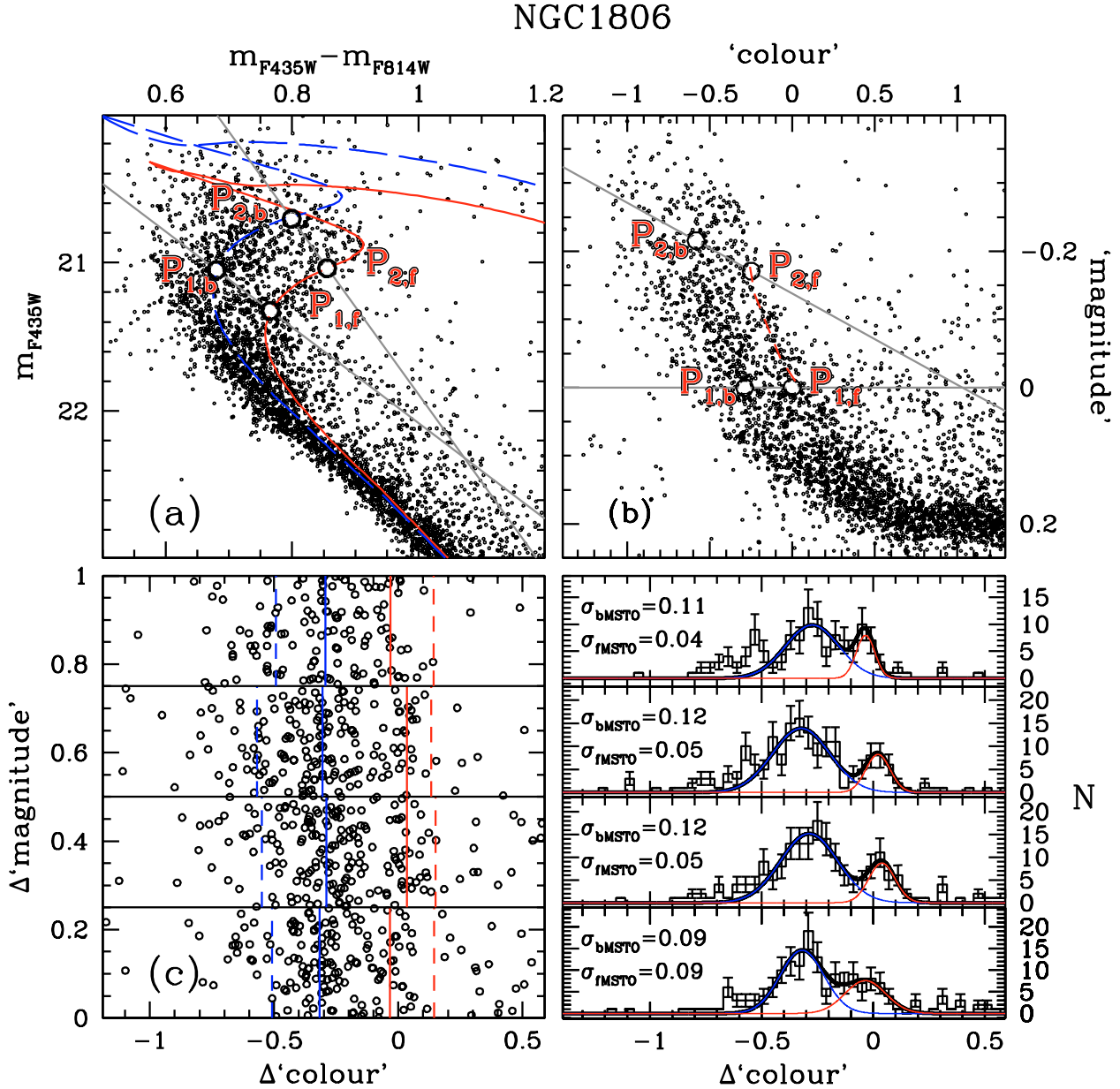


**Fig. 10.** Procedure adopted to measure the fraction of stars belonging to the  $b$ MSTO and  $f$ MSTO in NGC 1806. Panel a) shows a zoom of the CMD from Fig. 8 with the isochrones that best fits the  $f$ MSTO and the  $b$ MSTO superimposed. The grey lines delimit the portion of the CMD where the split is more evident. Only stars from this region are used to measure the population ratio. In Panel b) we shifted and rotated the reference frame of Panel a). Red dashed line is the fiducial of the region around the  $f$ MSTO. In Panel c) we plotted stars between the grey lines but after the subtraction of the “colour” of the region around the  $f$ MSTO fiducial from the “colour” of each star and the division of the “magnitude” of each star by the “magnitude” of the upper grey line. The four right bottom panels show the  $\Delta$  “color” distribution for stars in four  $\Delta$  “magnitude” bins. The solid lines represent a bi-Gaussian fit. For each bin, the dispersions of the best fitting Gaussians are indicated.

## 6. Does the spread MSTO reflect the presence of multiple stellar populations?

Globular-cluster systems with multiple populations manifest themselves in many different photometric ways. In  $\omega$  Cen we (Anderson 1997; Bedin et al. 2004) detected a split of the MS, which can only be explained by two stellar groups with different He content and metallicity (Piotto et al. 2005), and also at least four distinct SGBs (which may indicate age differences greater than 1 Gyr, see Villanova et al. 2007, and references within). In NGC 2808 we inferred the existence of three distinct stellar populations from the three MSs (which is most easily explained by three groups of stars with different helium content,

see Piotto et al. 2007). In the case of NGC 1851, two populations of stars are inferred from the fact that the SGB splitting into two branches. This feature can be explained either by two distinct bursts of star formation with a time separation of about 1 Gyr or by two stellar populations with distinct initial chemical composition and a much smaller age difference (Milone et al. 2008a; Cassisi et al. 2008). A split in the SGB has also been observed in NGC 6388 (Piotto 2008) demonstrating that this massive GC hosts two distinct stellar groups. In a spectro-photometric study of M4, Marino et al. (2008) detect a bimodal RGBs, and demonstrate that it is due to a bimodal distribution of CN, Na, O, also indicating that this relatively-small cluster contains multiple populations.

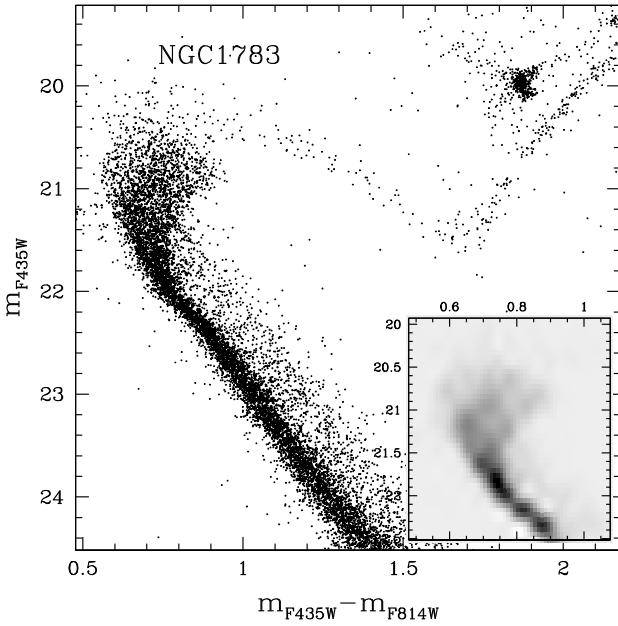


Fig. 11. As in Fig. 7 for NGC 1783.

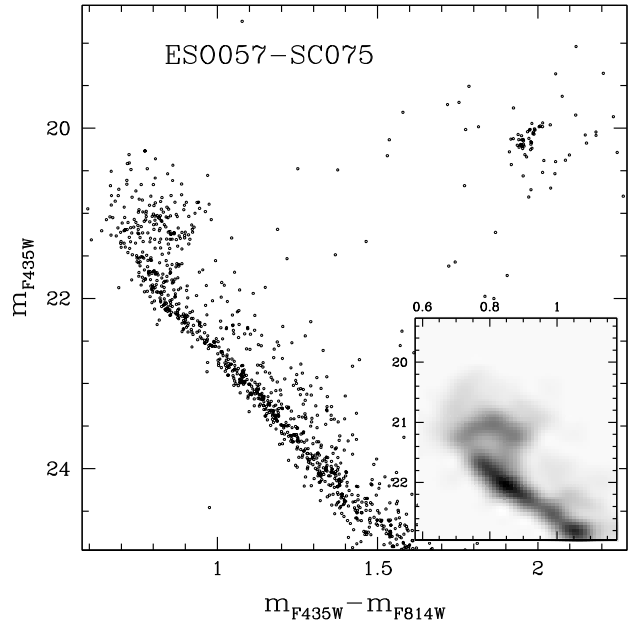


Fig. 12. As in Fig. 7 for ESO057-SC075.

The Galactic clusters cited above variously exhibit broadening or bifurcation of the RGB, SGB, and lower MS populations. In the case of the intermediate-age LMC clusters we studied here, we detected both splits of the MSTO, as in NGC 1846 and NGC 1806 (Sect. 4, M07 and M08), in NGC 1751 and possibly NGC 1783 (Sect. 4), and a broadening of the MSTO as the clusters in Figs. 12–14 and NGC 2173 (Bertelli et al. 2003). The low numbers of stars on the RGB make it difficult to assess the presence of a split or anomalous broadening along this evolutionary sequence, and the distance of the LMC makes it impossible to detect splits in the lower MS population with the presently available data.

While the splits and broadening we have shown above look quite convincing, it is important to consider the possibility that photometric errors or other effects can generate anomalous spreads and bifurcations, which could be confused with differences in age and/or chemical composition. In addition, it is also important to consider that both binaries and field stars contaminate the CMD region around the MSTO where we are most sensitive to the presence of multiple stellar populations.

In Sect. 6.1, we demonstrate that the MSTO broadening visible in Figs. 12–14 is not due to field-star contamination by statistically subtracting field stars from the cluster CMD. In Sect. 6.2, we consider the influence that binary stars could have on the spread of the MSTO. To do this, we use of artificial stars to simulate the CMD of a single population plus a population of binaries such that visible in the lower main sequence. We then present the decontaminated cluster CMD and compare it with the simulated one that includes both realistic errors and binaries to show that the observed MSTO broadening cannot be explained by a single population.

### 6.1. A method to decontaminate the cluster CMD from field stars

We began our analysis looking at the original CMD from stars near the cluster centre, where we estimated that the contamination by field stars is at most at the level of  $\sim 20\%$  (see Sect. 3).

However, it is possible to reduce this contamination even further by a statistical subtraction of those stars that are most likely to be field stars. We used the following approach which is based on the assumption that the distribution of field stars in the CMD of the cluster and reference field is nearly the same. For each star in the reference field CMD, we calculated the distance to all the cluster field stars:  $d = \sqrt{(\Delta(m_{F435W} - m_{F814W}))^2 + (\Delta m_{F435W})^2}$  (or  $d = \sqrt{(\Delta(m_{F555W} - m_{F814W}))^2 + (\Delta m_{F555W})^2}$ ). We then flagged the closest cluster field star as a candidate to be subtracted. We remind the reader that cluster and reference fields cover the same area.

We determined the ratio  $r$  between the completeness of this stars and the completeness of the reference field star. This ratio is always  $r < 1.0$ . To avoid over-subtracting field stars, we generated a random number between 0 and 1, and removed the star from the cluster CMD whenever this random number was less than the ratio of the completenesses.

The main steps in this procedure are illustrated in Fig. 24 for NGC 1806. The upper panels show the CMD of stars in the reference (left) and cluster (right) field, the bottom ones the CMD of subtracted stars (left), and the decontaminated CMD (right). The statistical subtraction of field stars was not applied to the most populated clusters (NGC 1978, NGC 1783), which occupy most of the field of view and have the highest ratio of cluster to reference field stars. We note that there is an additional young stellar cluster within the ACS images of NGC 1852, so we were careful to select a reference field that was as far as possible from both clusters.

Obviously, small variations in the distribution of stars in the reference field are expected even within the small WFC/ACS field of view. To check whether the reference field star distribution can be reasonably assumed uniform, we defined four regions with the same area of the cluster field and the largest possible distance from the cluster centre. We extracted the CMD of each region and compared it with that of the cluster field. A typical example of this procedure is shown in Fig. 25 for NGC 1987. In particular, we compared the number of stars (corrected for completeness) in the boxed region around the MSTO. We found that,

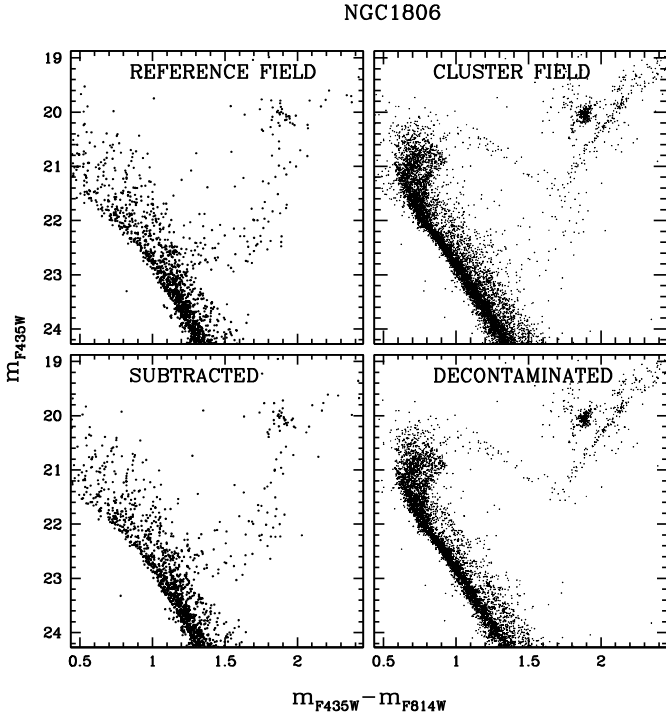


**Fig. 24.** Statistical decontamination from field stars of the CMD of NGC 1806. *Upper panels:* CMD extracted from the reference (*left*), and cluster fields (*right*). *Bottom panels:* CMD of all the stars that have been subtracted from the reference field (*left*) and decontaminated cluster CMD (*right*).

in most cases, the variation in the number of stars in this region is smaller than about 30%. Obviously, this procedure has been applied only to clusters that cover a sufficiently small fraction of the ACS field of view. We cannot exclude the possibility that the variation of the number of stars in reference field regions could be (partially) due to contamination of cluster members. However, we note that oversubtracting the cluster members does not affect our results for the morphology of the MSTO.

## 6.2. The synthetic CMD

The main goal of this section is to generate a synthetic CMD of a cluster with the same characteristics as the observed one, but hosting a single stellar population. This is a necessary step for demonstrating whether the observed spread in color around the MSTO is an intrinsic feature due to the multiple stellar populations or is an artifact produced by unresolved binaries or photometric errors.

To simulate a CMD that reproduces the main properties of the observed one well enough we must ensure that:

- the mass function of the synthetic CMD is as similar as possible to the observed one;
- simulated and observed stars have the same radial distribution, completeness, and photometric errors;
- the fraction and the mass ratio distribution of simulated photometric binaries are as close as possible to the real ones.

In the following we describe the procedure used to generate a synthetic CMD with these requirements. It consists of two main steps: in the first one we generate single stars; in the second one we measure the fraction of photometric binaries in the observed CMD and add the corresponding number of binary systems to the simulated CMD.

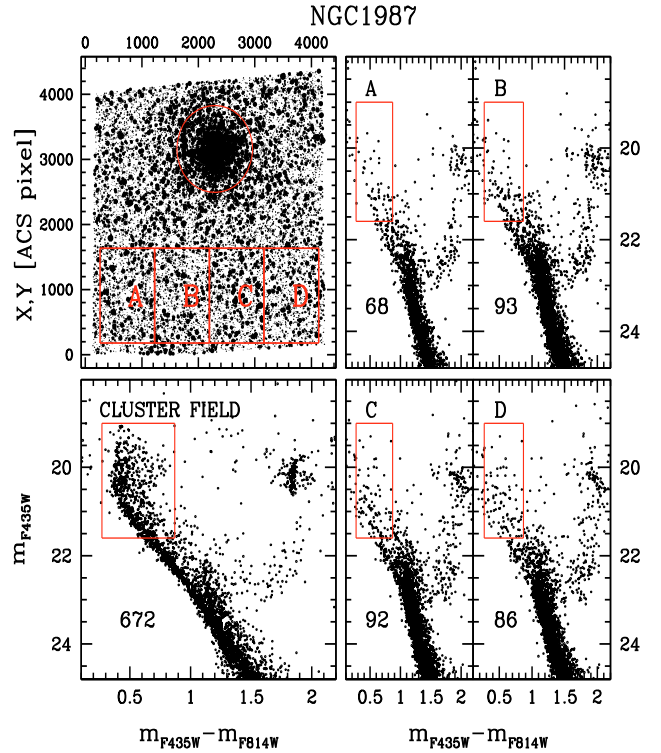


**Fig. 25.** Comparison of the CMD of the cluster field and those of four external reference regions (A, B, C and D) for NGC 1987. The values given in the bottom left corner of each CMD are the number of stars (corrected for incompleteness) in the box around the cluster MSTO.

### 6.2.1. Step one: simulation of single stars

We separately simulated MS and evolved stars.

**UNEVOLVED STARS:** to generate single MS stars we started by selecting a subsample of artificial stars with the following criterion. For each star in the cluster field that survived to the statistical subtraction of reference field stars of Sect. 6.1, we have assigned a subsample of the artificial stars and randomly extracted a star from it (see Sect. 2.2 for a description of how AS were generated). The artificial-star subsample consists of all the artificial stars with similar magnitudes (within 0.1  $m_{F814W}$  mag) and radial distances (less than 50 pixel from the observed star). This method produces a catalogue of simulated stars with almost the same luminosity, and radial distribution of the observed catalogue. This procedure has been applied only to MS stars.

**EVOLVED STARS:** things become more complicated for stars brighter than the MSTO where the complex shape of the CMD makes it harder to associate a star with the CMD sequence that corresponds to its evolutionary phase. For this reason, a different approach was used to simulate evolved stars (i.e. stars brighter than the MSTO).

First of all, we counted the number of MS stars (corrected for completeness) with  $m_{F814W}^{TO} < m_{F814W} < m_{F814W}^{TO} + 0.5$  and calculated the average number of stars per unit mass  $N_M$  in this range of luminosity. Next, we obtained  $N_M$  for stars brighter than the MSTO by using a Salpeter (1955) IMF and associated these stars to each portion of the CMD according to the Pietrinferni et al. (2004) models.

Since evolved stars should all have nearly the same mass, we would expect them to also have the same radial distribution. For this reason, we randomly associated the radial distance of an

observed star brighter than the MSTO to each simulated evolved star. Finally, for each simulated star, we selected the sample of artificial stars with almost the same magnitude, colour and distance from the cluster centre (we imposed that both input  $m_{F814W}$  magnitude and colour must differ by less than 0.01 mag and radial distance by less than 50 pixels) and randomly extracted a star from it.

It must be noted that the simulated CMDs have photometric errors that are slightly smaller than the errors of real stars. This reflects a fundamental limitation of artificial-star tests. An artificial star is measured by using the same PSF as was used to generate it, while for the real stars we necessarily have an imperfect PSF. The PSF is constructed to fit the real stars as closely as possible, but there will invariably be errors in the PSF model for the real stars, which will not be present for the artificial stars. (However, it must be clearly stated that these differences are appreciable only for the stars with the highest S/N ratio.)

Below, we describe the method we used to estimate the difference between the photometric errors of real and artificial stars. This allows us to introduce an additional error component in to the artificial-star photometry so that the real and artificial sequences can be directly compared. We illustrate the procedure for the case of NGC 1806. The same procedure was applied for all clusters.

To determine how much artificial broadening of the error distribution is necessary, we compare the color distribution of the observed and simulated MS stars. Figure 26 shows the colour distribution of MS stars for NGC 1806: the left panel contains the CMD of all the stars contained in the cluster field after the subtraction of the reference field stars. The red fiducial line (MSRL) is computed by using the following procedure. We started by dividing the CMD into bins of magnitude in the  $F814W$  band and, for each bin, we calculated the median colour and magnitude and obtained a raw fiducial line by fitting these points with a spline. Then for each star we derived the absolute value of the difference between its colour and the colour of the fiducial line, and calculated the  $\sigma$  as the 68.27th percentile. All the stars with distances greater than  $N\sigma$  from the fiducial were rejected and the survivors used to redetermine the median colour, magnitude, and  $\sigma$ . We iterated this procedure five times with  $N$  going from 6 to 2 (integer numbers).

In the middle panel we show the straightened CMD obtained by subtracting the color of the fiducial line from the color of each star. In the right panel we show the histograms of the color distribution in eight  $m_{F814W}$  magnitude intervals. The distribution in color is reproduced well by a Gaussian plus a tail on the red side due to the conspicuous number of photometric binaries and blends.

In Fig. 27 we also reproduce the distribution in colour for the artificial star MS. As expected, the spread of the latter is slightly less than that of the observed MS. We note that this additional dispersion does not allow us to exclude intrinsic dispersion of the MSs smaller than 0.03 mag in color, which might result from dispersion of  $Z$ ,  $Y$ , or a combination of the two (see discussion in Milone et al. 2008a). In Fig. 28 we compare the dispersions of the observed MS ( $\sigma_{\text{OBS}}$ , circles) and for artificial stars ( $\sigma_{\text{ART}}$ , triangles) as a function of the  $m_{F814W}$  magnitude. The continuous lines are the best-fitting fourth-order polynomials ( $P_{\text{OBS}}$  and  $P_{\text{ART}}$ ). Finally, we added to the color of each star of the artificial-star CMD an error randomly extracted from a Gaussian distribution with dispersion:  $P_{\text{DIF}} = \sqrt{P_{\text{OBS}}^2 - P_{\text{ART}}^2}$ .

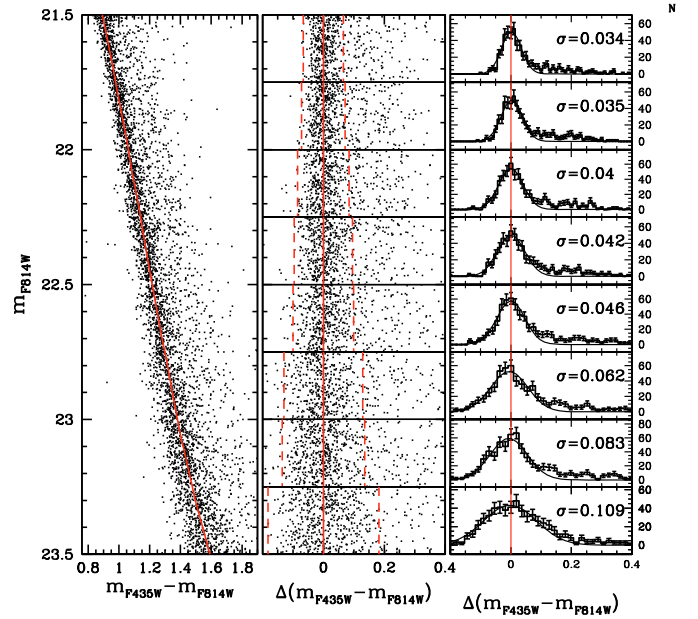


**Fig. 26.** *Left:* CMD of NGC 1806 with the MSRL overplotted; *middle:* the CMD rectified by subtraction of the MSRL; *right:* color distribution of the rectified CMD. The  $\sigma$  in the inset are those of the best-fitting Gaussians.

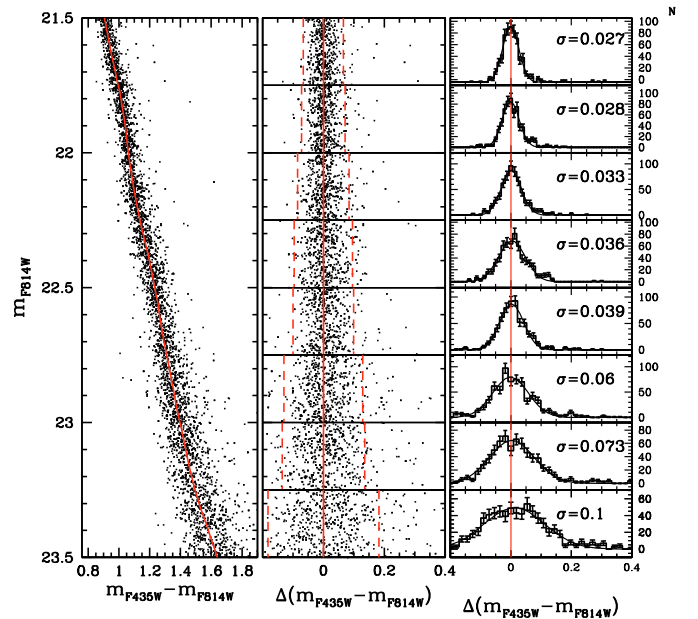


**Fig. 27.** As in Fig. 26 but for artificial stars.

## 6.2.2. Step two: simulation of binary systems

It is clear from the excess of stars on the red side of the main sequence that many of these clusters have sizeable binary populations (compare Figs. 26 with 27). We expect that this binary population can have some effect on the distribution of stars around the turnoff, so we estimate the binary-contamination effect. Binary stars of LMC clusters will be unresolved even with HST, but the light from each star will combine and the binary

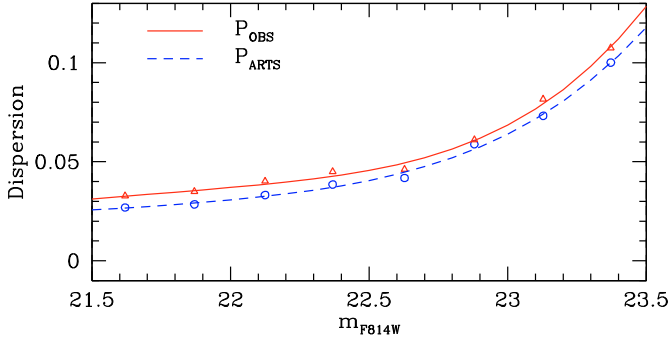


**Fig. 28.** Comparison of the  $\sigma$  of Gaussians that best fit the color distributions of MS stars in the observed (red triangles) and artificial stars (blue circles) CMD as a function of the  $m_{F814W}$  magnitude. Continuous and dashed lines are the best-fitting fourth-order polynomials.

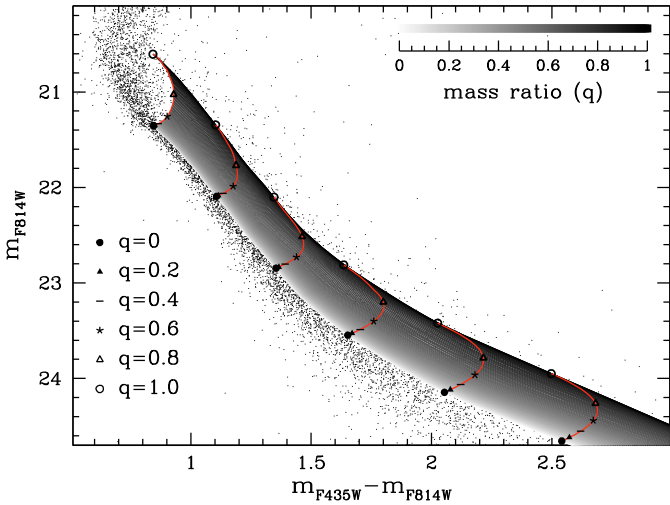


**Fig. 29.** CMD of NGC 1806. Grey area highlight the loci populated by MS-MS binaries. The levels of grey are proportional to the mass ratio. Red lines indicate the position of a MS-MS binary for six fixed values of the mass of the primary star ( $m_1$ ) and  $q$  ranging from 0 to 1.

system will appear as a single point-source object. These binaries can be discerned photometrically from the single stars along the MS as they are located brightward and to the red of the sequence. The position of the binary systems formed by two MS stars (MS-MS binaries) with different mass ratios in a typical CMD of an intermediate age LMC clusters are illustrated in Fig. 29.

In the same region of the CMD, in addition to the true physically associated binaries, we also expect a few chance superpositions (blends). The artificial-star tests (see Fig. 27) show that this is a very weak effect.

It is important to note here that measuring the fraction of binaries is not the goal of this paper. Instead, our aim here is to estimate their fraction so that we can determine how much of the spread of the MSTO region can reasonably be attributed to them.

Binaries can be parametrized by their mass ratio,  $q = m_1/m_2$ , where  $m_1 < m_2$ . To estimate the fraction of MS-MS photometric binaries with a mass ratio greater than a threshold value (hereafter  $q_{th}$ , see Table 2 for the adopted  $q_{th}$  for each cluster), we applied the methods described in Milone et al. (2008b) and Bedin et al. (2008). We divided the CMD into two regions: the first one (A) contains all the single MS stars and binaries with a primary star with  $(m_{F814W}^{MSTO} + 0.4) < m_{F814W} < (m_{F814W}^{MSTO} + 2.4)$  (where  $m_{F814W}^{MSTO}$  is the magnitude of the MSTO in the  $F814W$  band). It

**Table 2.** Fraction of photometric binaries with  $q > q_{th}$  and total fraction of binaries (Cols. 5 and 6) within the cluster field.

| ID           | $q_{th}$ | $f_{bin}^{q>q_{th}}$ | $f_{bin}^{TOT}$ |
|--------------|----------|----------------------|-----------------|
| ESO057-SC075 | 0.6      | $0.17 \pm 0.02$      | $0.42 \pm 0.05$ |
| HODGE7       | 0.7      | $0.08 \pm 0.01$      | $0.27 \pm 0.04$ |
| NGC 1644     | 0.7      | $0.09 \pm 0.02$      | $0.29 \pm 0.06$ |
| NGC 1652     | 0.7      | $0.06 \pm 0.01$      | $0.19 \pm 0.04$ |
| NGC 1751     | 0.6      | $0.13 \pm 0.01$      | $0.33 \pm 0.03$ |
| NGC 1795     | 0.7      | $0.12 \pm 0.02$      | $0.39 \pm 0.06$ |
| NGC 1806     | 0.6      | $0.13 \pm 0.01$      | $0.32 \pm 0.03$ |
| NGC 1852     | 0.7      | $0.11 \pm 0.02$      | $0.36 \pm 0.05$ |
| NGC 1917     | 0.7      | $0.09 \pm 0.02$      | $0.31 \pm 0.05$ |
| NGC 1987     | 0.6      | $0.12 \pm 0.01$      | $0.31 \pm 0.03$ |
| NGC 2108     | 0.6      | $0.18 \pm 0.01$      | $0.46 \pm 0.03$ |
| NGC 2154     | 0.7      | $0.08 \pm 0.01$      | $0.28 \pm 0.04$ |

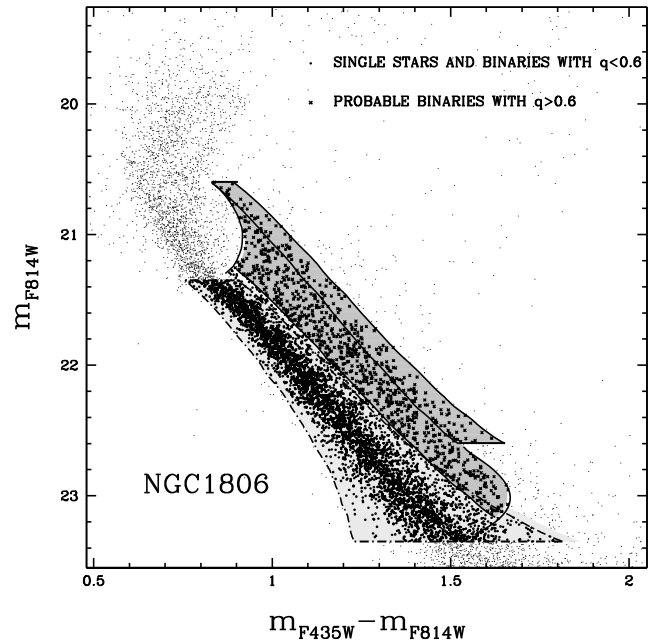


**Fig. 30.** The MS of NGC 1806 with the candidate binaries with mass ratio  $q > 0.6$  plotted as crosses.

corresponds to the light and dark grey areas of Fig. 30. The second region (B) is the part of A that contains MS-MS binaries with  $q > q_{th}$ , and corresponds to the dark grey area of Fig. 30. We adopted  $q_{th} = 0.6$  or  $q_{th} = 0.7$ , as indicated in Table 2, depending on the photometric quality of the data. The fraction of binaries with  $q > q_{th}$  has been evaluated as

$$f_{BIN}^{q>q_{th}} = \frac{N_{CLUSTER}^B - N_{REFERENCE}^B}{N_{CLUSTER}^A - N_{REFERENCE}^A} - \frac{N_{ARTS}^B}{N_{ARTS}^A}$$

where  $N_{CLUSTER}^{A(B)}$  is the number of stars (corrected for completeness) observed in the region A (B) of the CMD extracted from the cluster field,  $N_{REFERENCE}^{A(B)}$  are the corresponding numbers of stars in the CMD of the reference field and account for the field contamination and  $N_{ARTS}^{A(B)}$  refers to artificial stars: their ratio indicates the fraction of blends. Finally, we calculated the global fraction of binaries by interpolation, assuming a flat mass-ratio distribution. The only differences from Milone et al. (2008b) and Bedin et al. (2008) is that in this paper we removed the contribution from field stars by using the CMD observed in the reference

region, rather than by using a Galactic model or proper motions. The measured fraction of binaries in each cluster are in Table 2.

We tried very hard to get a reliable binary fraction for those clusters, but unfortunately, they are just too big on ACS/WFC FOV. If we take the outskirts as representative of the field, we would end up subtracting cluster members from clusters, and since energy equipartition makes the binary sink into the cluster core, this could potentially generate dangerous biases in the relative fraction of a single to binary system. We avoid on purpose to giving numbers in Table 1 for those clusters, to avoid contamination of the literature with unreliable values of the binary fraction for those objects.

To simulate binary stars to be added to the simulated CMD described in Sect. 6.2 we adopted the following procedure:

- we selected a fraction  $F_{\text{BIN}}$  of single stars equal to the measured fraction of binaries and derived their masses by using the Pietrinferni et al. (2004) mass-luminosity relation. For the clusters where the measure of the binary fraction is not available, we assumed the average value of  $F_{\text{BIN}} = 0.33$ ;
- for each of them, we calculated the mass  $M_2 = q \times M_1$  of the secondary star and obtained the corresponding  $m_{F814W}$  magnitude. Its colour was derived by the MSRL;
- finally, we summed up the  $F435W$  (or  $F555W$ ) and  $F814W$  fluxes of the two components, calculated the corresponding magnitudes, added the corresponding photometric error, and replaced the original star in the CMD with this binary system.

Figures 31–34 show the contribution that we would expect from binaries to the broadening of the cluster TOs. It is clear that the double MSTO in NGC 1806, NGC 1846, and NGC 1751, and the extended (broadened) MSTO in ESO057-SC075, HODGE 7, NGC 1783, NGC 1852, NGC 1917, NGC 1987, NGC 2108, and NGC 2154 are intrinsic features of these objects, and cannot be due to field-star contamination, photometric errors, or binaries. In these figures, we show, from the left to the right, a zoom of the original cluster-field CMD around the MSTO, the same portion of the CMD but for stars in the reference field, the CMD after field-star decontamination, and the simulated CMD for these clusters.

Figures 35 and 36 illustrate the same exercise for the clusters with no significant MSTO broadening. Now that we have introduced the simulated CMDs, we can describe how we distinguish between clusters that show evidence of hosting a multiple population, and those that do not. First, we calculated the dispersion of stars along the same direction perpendicular to the observed spread (on the right of the MSTO) for real ( $\sigma_{\text{SGB}}^{\text{OBS}}$ ) and artificial stars ( $\sigma_{\text{SGB}}^{\text{ART}}$ ). Then, we considered a cluster as hosting a multiple population if the dispersion of real stars was more than three times the dispersion of the simulated CMD. This condition is verified for eleven out of the sixteen clusters. Although the exact position of the line along which to measure the spread is not unique, it seemed to us a reasonably solid approach.

## 7. Isochrone fitting

Both M07 and M08 propose that the split of the MSTO of NGC 1846 and NGC 1806 is consistent with the presence of two distinct stellar populations with the same chemical composition and a difference in age of about  $\sim 300$  Myr. In addition, M08 suggest that the spread of the MSTO of NGC 1783 can be attributed to a prolonged star formation.

In the previous sections, we demonstrated that eight additional clusters show strong indications of an intrinsic spread or

split of the CMD around the MSTO region. The remaining five objects of our sample show no significant evidence of a multiple stellar population within our photometric precision (see Figs. 35 and 36).

We note that in the clusters where a spread in the MSTO is claimed, the other evolutionary sequences are narrow and well defined, after a correction for differential reddening has been made. The tightness of these other sequences is also a strong indication that there is very little variation in metallicity among the stars.

Therefore, in the absence of any detailed chemical composition analysis, we will assume in what follows that any spread around the MSTO can be attributed to a difference in age alone. We derive the main parameters for each cluster (metallicity, age, and the maximum age spread among the populations) by fitting the data with the isochrones from the BaSTI evolutionary code (Pietrinferni et al. 2004, updated version of August 2008). Each of the isochrones has a solar-scaled distribution of metals and includes convective overshooting.

To determine the isochrone that best matches the observed CMD of our clusters with no evidence of an intrinsic spread around the MSTO, we followed a procedure similar to the one adopted by M07. We generated a grid of isochrones using metallicities of  $Z = 0.008$  and  $0.010$ , sampling an age range between 1.0 and 3.0 Gyr at intervals of 0.05 Gyr. Then, we defined by hand the magnitude of the MSTO, the color of the RGB at a level intermediate between that of the red end of the SGB and that of the HB red-clump, and the magnitude of the HB red-clump. In this way we calculated the difference in magnitude between the MSTO and the HB red-clump ( $\Delta_{\text{mag}}$ ) and the difference in color between the MSTO and the fiducial points on the RGB ( $\Delta_{\text{col}}$ ). Then we calculated a value of  $\Delta_{\text{mag}}$  and  $\Delta_{\text{col}}$  for each isochrone in the grid and compared them with the observed ones. Finally, we selected all the isochrones where  $\Delta_{\text{col}}$  and  $\Delta_{\text{mag}}$  differ respectively by less  $\pm 0.25$  and  $\pm 0.03$  mag and fitted them to the CMD by hand. To do this, we varied the distance modulus in the range  $18.30 < (m-M)_0 < 18.70$  and the reddening between 0.00 and 0.30, both in steps of 0.01 mag and searched for the combination that matches the cluster sequences best. For clusters with a double or broadened MSTO, we used a similar approach with the exception that, in this case, we first defined on the observed CMD the magnitude of the MSTO and the values of  $\Delta_{\text{mag}}$  and  $\Delta_{\text{col}}$  for the  $b$ MSTO and determined the isochrone that best fits this younger population. Then, we selected all the isochrones with the same metallicity, distance modulus, and reddening, but different ages, and fitted the  $f$ MSTO. For clusters with a broadened MSTO, we calculated those values that correspond to the brighter and the fainter region of the MSTO.

The best fitting distance modulus, reddening, metallicity, and age are listed in Table 3. The last column indicates the maximum age difference,  $\Delta_{\text{age}}$ , for stars in clusters that show possible evidence of multiple or prolonged star formation episodes. In Figs. 37–39, we have overplotted the best fitting isochrones to the observed CMDs. Interestingly, the multiple (or prolonged) star-formation episodes seem to lie between 150 and 250 Myr, which is very similar to the time interval between successive star formation episodes in the intermediate-mass AGB star ejecta pollution depicted by Ventura et al. (2001).

## 8. Conclusions

High-precision HST ACS/HST photometry of sixteen intermediate age LMC stellar clusters has revealed that eleven of them

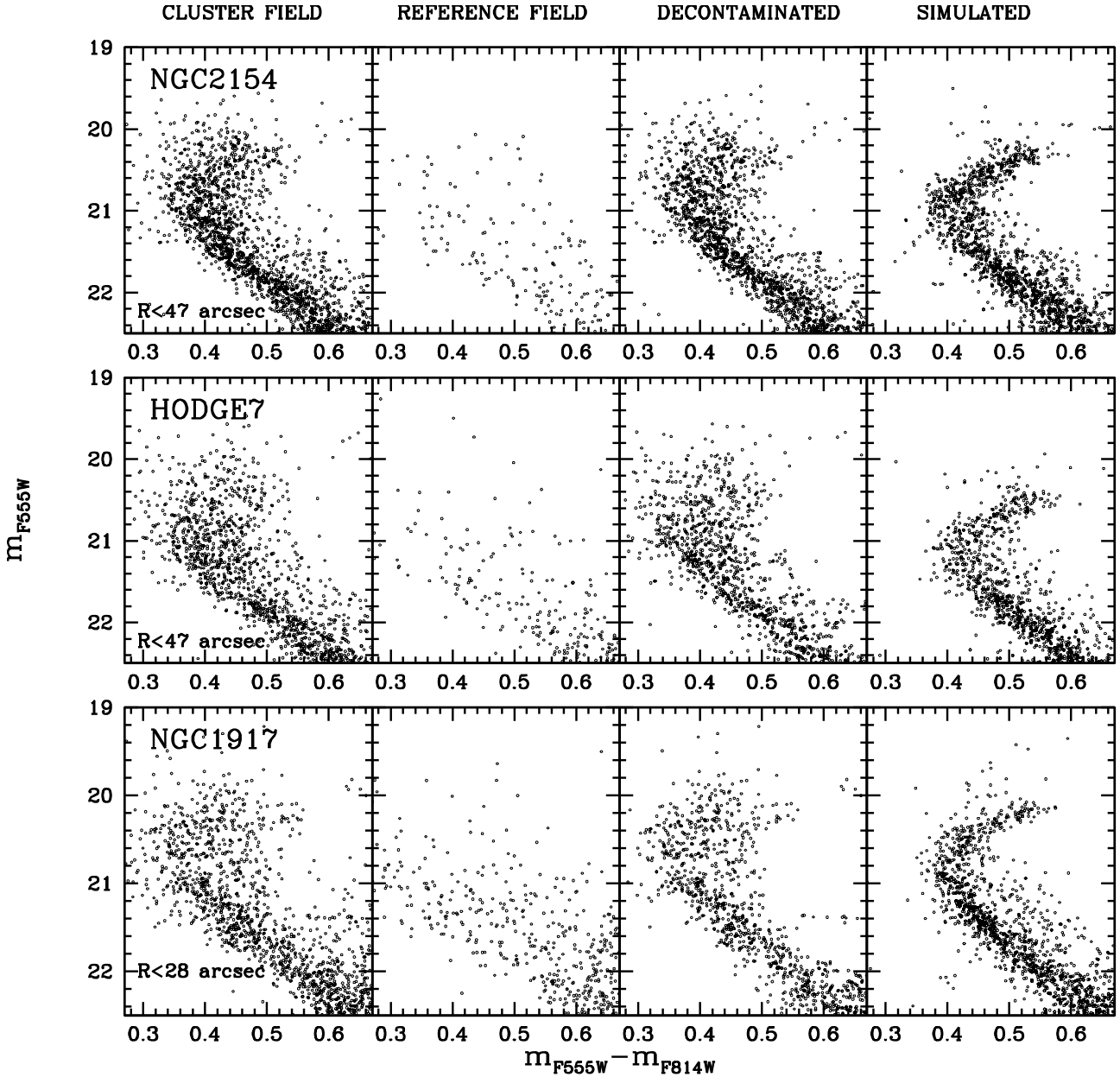


**Fig. 31.** From left to right in each column: CMD of the cluster field for NGC 2154, HODGE 7, and NGC 1917, CMD of the reference field, CMD of the cluster field after the reference field stars have been statistically subtracted, simulated CMD.

(i.e. about the  $70 \pm 25\%$  of the entire sample) host multiple stellar populations.

The CMDs of NGC 1806, NGC 1846, and NGC 1751 exhibit two distinct MSTOs, suggesting that these clusters have experienced (at least) two main episodes of star formation with a temporal separation of 200–250 Myr. For these three clusters, the high quality of our photometry enabled us not only to distinguish the two populations, but also to measure the fraction of stars belonging to each of them. In all these cases, the population corresponding to the brighter MSTO (the younger population) is the main population, and it includes more than two-thirds of the cluster stellar population, consistent with the intermediate mass AGB pollution scenario (See D’Antona & Caloi 2008, for a recent review).

Our photometry strongly suggests that the intrinsic broadening of the MSTO of NGC 1783 observed by M08 could be

**Table 3.** Parameters that have been used to obtain the best fit between the observed CMD and the BaSTI isochrones.

| ID           | $(m - M)_0$ | $E(B - V)$ | $Z$   | Age (Myr) | $\Delta_{\text{age}}$ |
|--------------|-------------|------------|-------|-----------|-----------------------|
| ESO057-SC075 | 18.46       | 0.14       | 0.008 | 1400–1600 | $200 \pm 50$          |
| HODGE7       | 18.48       | 0.04       | 0.008 | 1400–1550 | $150 \pm 50$          |
| IC2146       | 18.50       | 0.07       | 0.008 | 1550      | <50                   |
| NGC 1644     | 18.48       | 0.01       | 0.008 | 1550      | <50                   |
| NGC 1652     | 18.48       | 0.06       | 0.008 | 1700      | <50                   |
| NGC 1751     | 18.45       | 0.22       | 0.008 | 1300–1500 | $200 \pm 50$          |
| NGC 1783     | 18.46       | 0.06       | 0.008 | 1400–1600 | $200 \pm 50$          |
| NGC 1795     | 18.45       | 0.10       | 0.008 | 1300      | <50                   |
| NGC 1806     | 18.44       | 0.09       | 0.008 | 1400–1600 | $200 \pm 50$          |
| NGC 1846     | 18.49       | 0.09       | 0.008 | 1350–1600 | $250 \pm 50$          |
| NGC 1852     | 18.50       | 0.08       | 0.008 | 1200–1450 | $250 \pm 50$          |
| NGC 1917     | 18.48       | 0.08       | 0.008 | 1200–1350 | $150 \pm 50$          |
| NGC 1978     | 18.49       | 0.09       | 0.008 | 2000      | <100                  |
| NGC 1987     | 18.40       | 0.04       | 0.010 | 950–1200  | $250 \pm 50$          |
| NGC 2108     | 18.40       | 0.21       | 0.010 | 950–1100  | $150 \pm 50$          |
| NGC 2154     | 18.48       | 0.04       | 0.008 | 1350–1500 | $150 \pm 50$          |

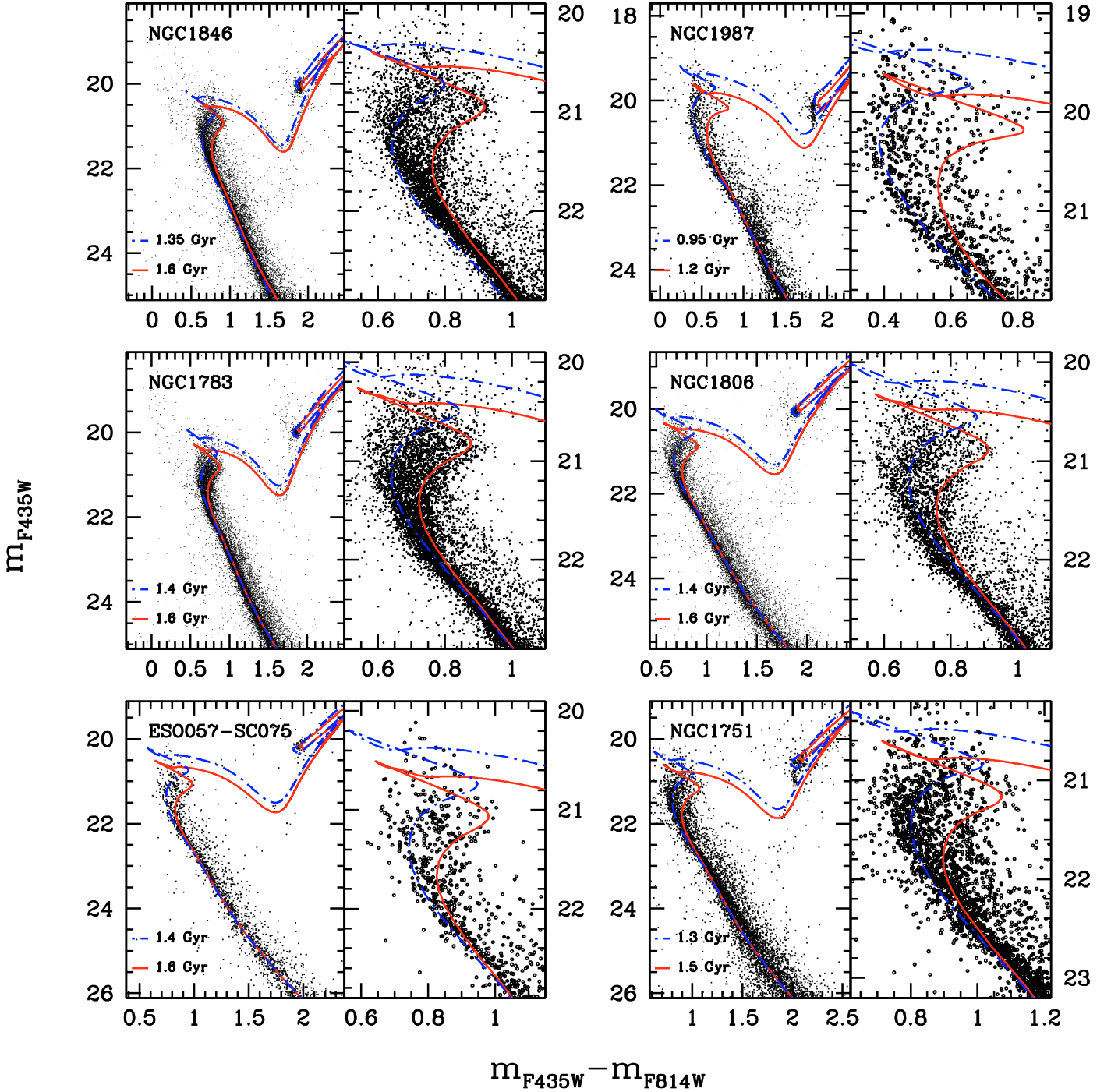


**Fig. 37.** The best-fitting isochrones, obtained by using the distance modulus, reddening, metallicity, and age(s) of NGC 1846, NGC 1987, NGC 1783, NGC 1806, ESO057-SC075, and NGC 1751 listed in Table 3 and overplotted on the CMD of the cluster field of (left). A zoom of the region around the MSTO is shown on the right.

attributed to the presence of two distinct branches that are closely spaced and poorly resolved by the observations.

In seven additional clusters, namely ESO057-SC075, HODGE7, NGC 1852, NGC 1917, NGC 1987, NGC 2108, and NGC 2154, we observed a wide spread in colour for the stars around the MSTO. In spite of this, the other main features of the CMD are narrow and well-defined, demonstrating that the spread cannot be an artifact produced by differential reddening, by variation in the photometric zero point along the chip, or by a relatively wide spread in metallicity. By using the CMD of the stars in the fields that surround the cluster, we demonstrated that

the observed feature is unequivocally associated with the clusters. Finally, artificial stars and simulated CMDs show that the wide spread in colour observed around the MSTO cannot be produced by photometric errors or binaries. It is interesting to note that the age spreads observed in this sample appear to be quite similar, with all between 150 and 250 Myr.

*Acknowledgements.* We thank the anonymous referee for the careful reading of the manuscript and for the useful comments.

## References

- Anderson, J. 1997, Ph.D. Thesis, Univ. California, Berkeley
- Anderson, J., & King, I. R. 2006, ACS/ISR 2006-01, PSFs, Photometry and Astrometry for the ACS/WFC
- Anderson, J., Sarajedini, A., Bedin, L. R., et al. 2008, *AJ*, 135, 2055
- Bedin, L. R., Piotto, G., Anderson, J., et al. 2004, *ApJ*, 605, L125
- Bedin, L. R., Cassisi, S., Castelli, F., et al. 2005, *MNRAS*, 357, 1048
- Bedin, L. R., Salaris, M., Piotto, G., et al. 2008, *ApJ*, 679, L29
- Bertelli, G., Nasi, E., Girardi, L., et al. 2003, *AJ*, 125, 770
- Cassisi, S., Salaris, M., Pietrinferni, A., et al. 2008, *ApJ*, 672, L115
- D'Antona, F., & Caloi, V. 2008, *MNRAS*, accepted [arXiv:0807.4233]
- D'Antona, F., Bellazini, M., Caloi, V., et al. 2005, *ApJ*, 631, 868
- Glatt, K., Grebel, E. K., Sabbi, E., et al. 2008a, *AJ*, 136, 1703
- Glatt, K., Grebel, E. K., Sabbi, E., et al. 2008b, *AJ*, 135, 1106
- Gratton, R. G., Bonifacio, P., Bragaglia, A., et al. 2001, *A&A*, 369, 87
- Gratton, R. G., Sneden, C., & Carretta, E. 2004, *ARA&A*, 42, 385
- Mackey, A. D., & Broby Nielsen, P. 2007, *MNRAS*, 369, 921 (M07)
- Mackey, A. D., Broby Nielsen, P., Ferguson, M. N., & Richardson, J. C. 2008, *ApJ*, 681, L17 (M08)
- Marino, A. F., Villanova, S., Piotto, G., et al. 2008, *A&A*, 490, 625
- Milone, A. P., Bedin, L. R., Piotto, G., et al. 2008a, *ApJ*, 673, 241
- Milone, A. P., Piotto, G., Bedin, L. R., & Sarajedini, A. 2008b, in *XXI Century Challenges for Stellar Evolution*, Mem. Soc. Astron. Ital., 79/2, ed. S. Cassisi, & M. Salaris [arXiv:0801.3177]
- Mucciarelli, A., Origlia, L., & Ferraro, F. R. 2007, *AJ*, 134, 1813
- Pietrinferni, A., Cassisi, S., Salaris, M., & Castelli, F. 2004, *ApJ*, 612, 168
- Pietrinferni, A., Cassisi, S., Salaris, M., & Castelli, F. 2006, *ApJ*, 642, 797
- Piotto, G. 2008, in *XXI Century Challenges for Stellar Evolution*, Memorie della Societa Astronomica Italiana, vol. 79/2, ed. S. Cassisi, & M. Salaris [arXiv:0801.3175]
- Piotto, G., Villanova, S., Bedin, L. R., et al. 2005, *ApJ*, 621, 777
- Piotto, G., Villanova, S., Bedin, L. R., et al. 2007, *ApJ*, 661, L53
- Piotto, G. 2009, et al. in preparation
- Salpeter, E. 1955, *ApJ*, 121, 161
- Sarajedini, A., Barker, M. K., Geisler, D., Harding, P., & Schommer, R. 2007, *AJ*, 133, 290
- Sollima, A., Ferraro, F. R., Bellazzini, M., et al. 2007, *ApJ*, 654, 915
- Sirianni, M., Jee, M. J., Beni'tez, N., et al. 2005, *PASP*, 117, 1049
- Ventura, P., D'Antona, F., Mazzitelli, I., & Gratton, R. 2001, *ApJ*, 550, 65
- Villanova, S., Piotto, G., King, I. R., et al. 2007, *ApJ*, 663, 296
- Yong, D., Grundahal, F., Johnson, J. A., & Asplund, M. 2008 [arXiv:0806.0187v1]

**Table 1.** Description of the data sets.

| ID            | Date            | Exposures    | Filter | Program ID | ID        | Date         | Exposures    | Filter | Program |
|---------------|-----------------|--------------|--------|------------|-----------|--------------|--------------|--------|---------|
| ESO 057-SC075 | Nov. 05 2006    | 55 s+2×340 s | F435W  | 10 595     | NGC 1806  | Aug. 08 2003 | 300 s        | F555W  | 9891    |
|               | Nov. 05 2006    | 25 s+2×340 s | F555W  | 10 595     |           | Aug. 08 2003 | 200 s        | F814W  | 9891    |
|               | Nov. 05 2006    | 15 s+2×340 s | F814W  | 10 595     |           | Sep. 29 2005 | 90 s+2×340 s | F435W  | 10 595  |
| ESO 121-SC03  | Oct. 07 2003    | 330 s        | F555W  | 9891       |           | Sep. 29 2005 | 40 s+2×340 s | F555W  | 10 595  |
|               | Oct. 07 2003    | 200 s        | F814W  | 9891       |           | Sep. 29 2005 | 8 s+2×340 s  | F814W  | 10 595  |
| HODGE 7       | Oct. 07 2003    | 330 s        | F555W  | 9891       | NGC 1846  | Oct. 08 2003 | 300 s        | F555W  | 9891    |
|               | Oct. 07 2003    | 200 s        | F814W  | 9891       |           | Oct. 08 2003 | 200 s        | F814W  | 9891    |
| IC 1660       | Aug. 13 2003    | 73 s         | F555W  | 9891       |           | Jan. 01 2006 | 90 s+2×340 s | F435W  | 10 595  |
|               | Aug. 13 2003    | 58 s         | F814W  | 9891       |           | Jan. 01 2006 | 40 s+2×340 s | F555W  | 10 595  |
| IC 2146       | Jul. 07 2003    | 250 s        | F555W  | 9891       |           | Jan. 01 2006 | 8 s+2×340 s  | F814W  | 10 595  |
|               | Jul. 07 2003    | 170 s        | F814W  | 9891       |           | Oct. 07 2003 | 330 s        | F555W  | 9891    |
| KRON 1        | Aug. 27 2003    | 480 s        | F555W  | 9891       | NGC 1852  | Oct. 07 2003 | 200 s        | F814W  | 9891    |
|               | Aug. 27 2003    | 290 s        | F814W  | 9891       |           | Oct. 07 2003 | 50 s         | F555W  | 9891    |
| KRON 21       | Aug. 22 2003    | 480 s        | F555W  | 9891       | NGC 1854  | Oct. 07 2003 | 40 s         | F814W  | 9891    |
|               | Aug. 22 2003    | 290 s        | F814W  | 9891       |           | Oct. 08 2003 | 20 s         | F555W  | 9891    |
| KRON 34       | Aug. 12 2003    | 165 s        | F555W  | 9891       | NGC 1858  | Oct. 08 2003 | 20 s         | F814W  | 9891    |
|               | Aug. 12 2003    | 130 s        | F814W  | 9891       |           | Sep. 21 2003 | 115 s        | F555W  | 9891    |
| LYNDSAY 1     | Jul. 11 2003    | 480 s        | F555W  | 9891       | NGC 1872  | Sep. 21 2003 | 90 s         | F814W  | 9891    |
|               | Jul. 11 2003    | 290 s        | F814W  | 9891       |           | Jul. 02 2004 | 50 s         | F555W  | 9891    |
| LYNDSAY 38    | Jun. 03 2004    | 480 s        | F555W  | 9891       | NGC 1903  | Jul. 02 2004 | 40 s         | F814W  | 9891    |
|               | Jun. 03 2004    | 290 s        | F814W  | 9891       |           | Oct. 07 2003 | 300 s        | F555W  | 9891    |
| LYNDSAY 91    | Aug. 24 2003    | 435 s        | F555W  | 9891       | NGC 1917  | Oct. 07 2003 | 200 s        | F814W  | 9891    |
|               | Aug. 24 2003    | 290 s        | F814W  | 9891       |           | Aug. 23 2003 | 330 s        | F555W  | 9891    |
| LYNDSAY 113   | Jun. 03 2004    | 480 s        | F555W  | 9891       | NGC 1928  | Aug. 23 2003 | 200 s        | F814W  | 9891    |
|               | Jun. 03 2004    | 290 s        | F814W  | 9891       |           | Jul. 27 2003 | 330 s        | F555W  | 9891    |
| LYNDSAY 114   | Aug. 07 2003    | 480 s        | F555W  | 9891       | NGC 1939  | Jul. 27 2003 | 200 s        | F814W  | 9891    |
|               | Aug. 07 2003    | 290 s        | F814W  | 9891       |           | Oct. 07 2003 | 50 s         | F555W  | 9891    |
| NGC 265       | Aug. 24 2003    | 29 s         | F555W  | 9891       | NGC 1943  | Oct. 07 2003 | 40 s         | F814W  | 9891    |
|               | Aug. 24 2003    | 29 s         | F814W  | 9891       |           | Oct. 07 2003 | 115 s        | F555W  | 9891    |
| NGC 294       | Aug. 24 2003    | 165 s        | F555W  | 9891       | NGC 1953  | Oct. 07 2003 | 90 s         | F814W  | 9891    |
|               | Aug. 24 2003    | 130 s        | F814W  | 9891       |           | Oct. 07 2003 | 300 s        | F555W  | 9891    |
| NGC 422       | Oct. 07 2003    | 73 s         | F555W  | 9891       | NGC 1978  | Oct. 07 2003 | 200 s        | F814W  | 9891    |
|               | Oct. 07 2003    | 58 s         | F814W  | 9891       |           | Oct. 07 2003 | 20 s         | F555W  | 9891    |
| NGC 602       | Aug. 16 2003    | 29 s         | F555W  | 9891       | NGC 1983  | Oct. 07 2003 | 20 s         | F814W  | 9891    |
|               | Aug. 16 2003    | 29 s         | F814W  | 9891       |           | Oct. 07 2003 | 250 s        | F555W  | 9891    |
| NGC 1644      | Oct. 07 2003    | 250 s        | F555W  | 9891       | NGC 1987  | Oct. 07 2003 | 170 s        | F814W  | 9891    |
|               | Oct. 07 2003    | 170 s        | F814W  | 9891       |           | Oct. 18 2006 | 90 s+2×340 s | F435W  | 10 595  |
| NGC 1652      | Oct. 07 2003    | 300 s        | F555W  | 9891       | NGC 2002  | Oct. 18 2006 | 40 s+2×340 s | F555W  | 10 595  |
|               | Oct. 07 2003    | 200 s        | F814W  | 9891       |           | Oct. 18 2006 | 8 s+2×340 s  | F814W  | 10 595  |
| NGC 1751      | Oct. 07 2003    | 300 s        | F555W  | 9891       | NGC 2010  | Aug. 23 2003 | 20 s         | F555W  | 9891    |
|               | Oct. 07 2003    | 200 s        | F814W  | 9891       |           | Aug. 23 2003 | 20 s         | F814W  | 9891    |
|               | Oct. 17–18 2006 | 90 s+2×340 s | F435W  | 10 595     |           | Oct. 07 2003 | 20 s         | F555W  | 9891    |
|               | Oct. 17–18 2006 | 40 s+2×340 s | F555W  | 10 595     |           | Oct. 07 2003 | 20 s         | F814W  | 9891    |
| NGC 1755      | Oct. 17–18 2006 | 8 s+2×340 s  | F814W  | 10 595     | NGC 2056  | Aug. 08 2003 | 170 s        | F555W  | 9891    |
|               | Aug. 23 2003    | 50 s         | F555W  | 9891       |           | Aug. 08 2003 | 120 s        | F814W  | 9891    |
| NGC 1756      | Aug. 23 2003    | 40 s         | F814W  | 9891       | NGC 2107  | Oct. 07 2003 | 170 s        | F555W  | 9891    |
|               | Aug. 12 2003    | 170 s        | F555W  | 9891       |           | Oct. 07 2003 | 120 s        | F814W  | 9891    |
| NGC 1783      | Aug. 12 2003    | 120 s        | F814W  | 9891       | NGC 2108  | Aug. 16 2003 | 250 s        | F555W  | 9891    |
|               | Oct. 07 2003    | 250 s        | F555W  | 9891       |           | Aug. 16 2003 | 170 s        | F814W  | 9891    |
| NGC 1795      | Oct. 07 2003    | 170 s        | F814W  | 9891       | RETICULUM | Aug. 22 2006 | 90 s+2×340 s | F435W  | 10 595  |
|               | Jan. 01 2006    | 90 s+2×340 s | F435W  | 10 595     |           | Aug. 22 2006 | 40 s+2×340 s | F555W  | 10 595  |
|               | Jan. 01 2006    | 40 s+2×340 s | F555W  | 10 595     |           | Aug. 22 2006 | 8 s+2×340 s  | F814W  | 10 595  |
|               | Jan. 01 2006    | 8 s+2×340 s  | F814W  | 10 595     |           | Oct. 08 2003 | 300 s        | F555W  | 9891    |
| NGC 1801      | Aug. 09 2003    | 300 s        | F555W  | 9891       | RETICULUM | Oct. 08 2003 | 200 s        | F814W  | 9891    |
|               | Aug. 09 2003    | 200 s        | F814W  | 9891       |           | Sep. 21 2003 | 330 s        | F555W  | 9891    |
| NGC 1875      | Oct. 08 2003    | 115 s        | F555W  | 9891       | RETICULUM | Sep. 21 2003 | 200 s        | F814W  | 9891    |
|               | Oct. 08 2003    | 90 s         | F814W  | 9891       |           |              |              |        |         |

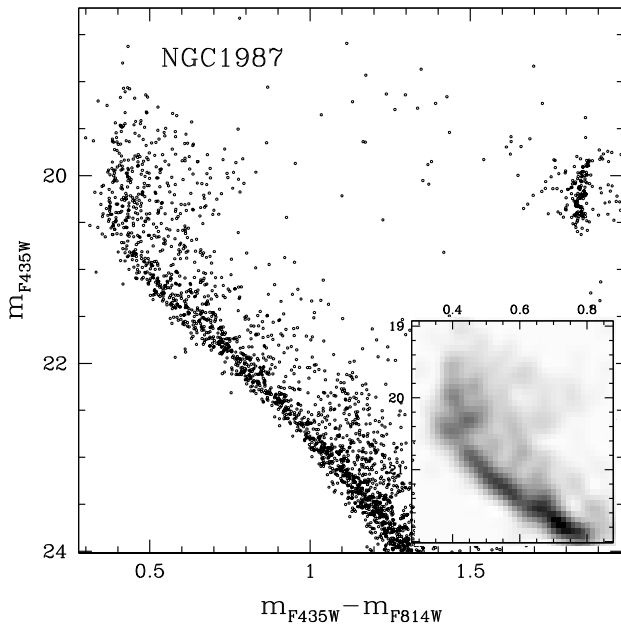


**Fig. 13.** As in Fig. 7 for NGC 1987.

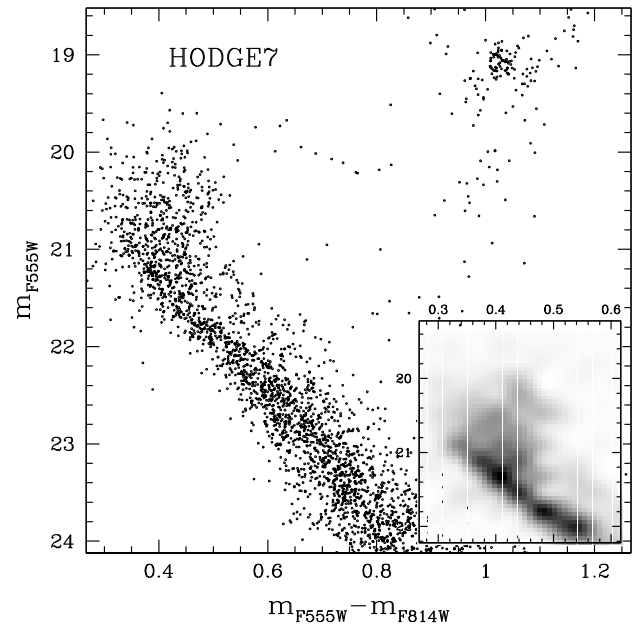


**Fig. 15.** As in Fig. 7 for HODGE 7.

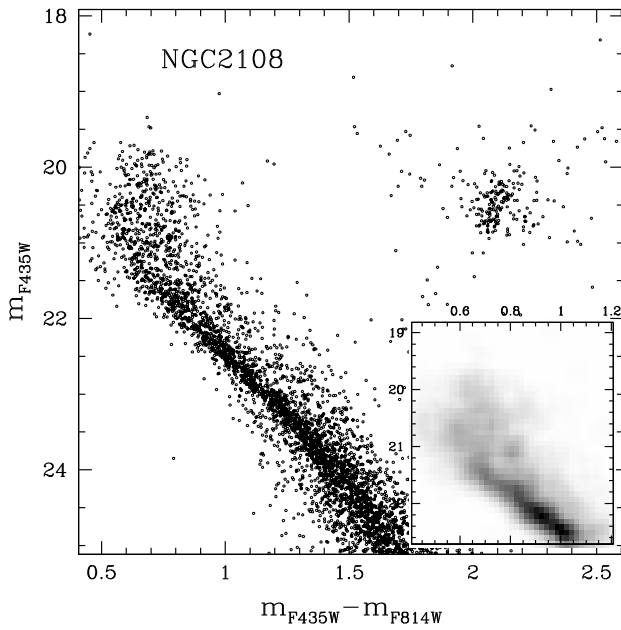


**Fig. 14.** As in Fig. 7 for NGC 2108.

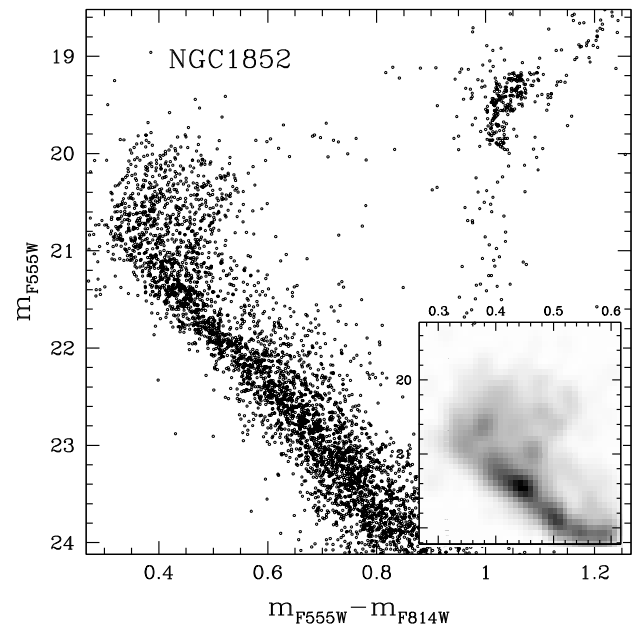


**Fig. 16.** As in Fig. 7 for NGC 1852.

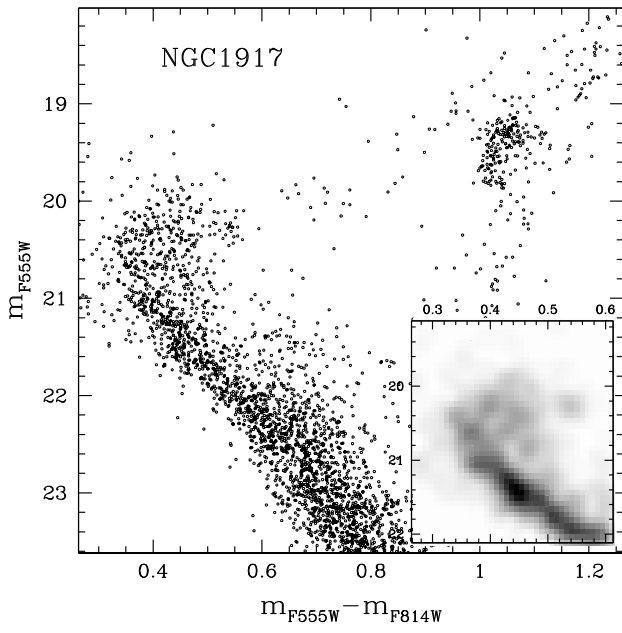


**Fig. 17.** As in Fig. 7 for NGC 1917.

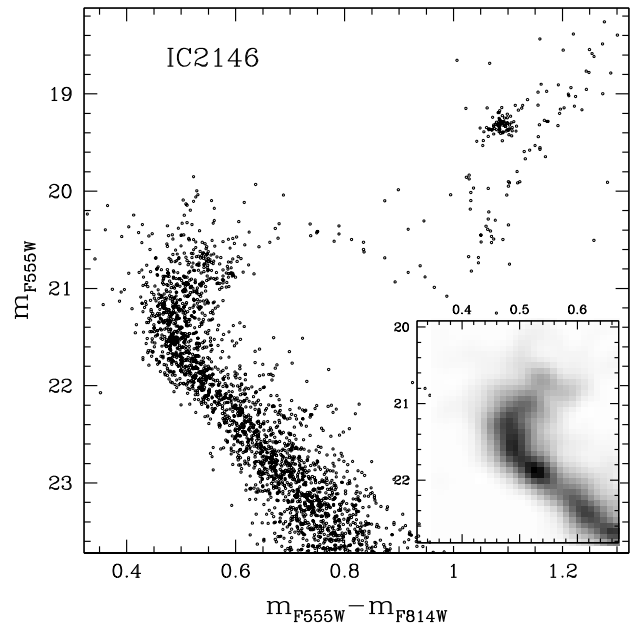


**Fig. 19.** As in Fig. 7 for IC 2146.

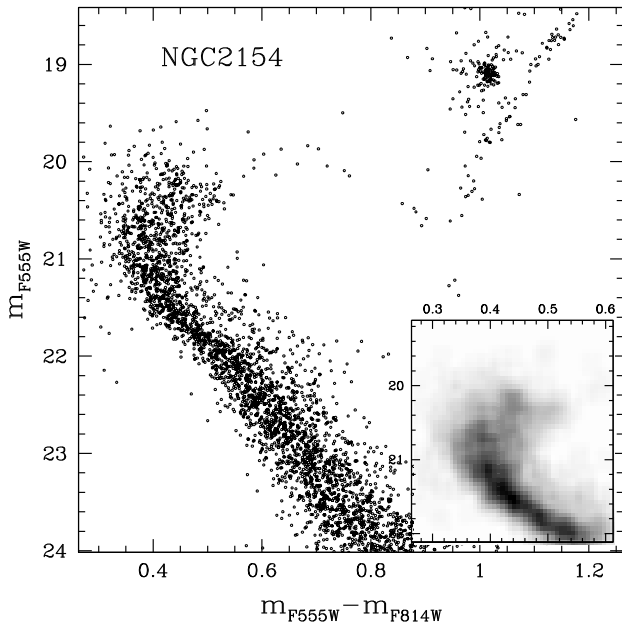


**Fig. 18.** As in Fig. 7 for NGC 2154.

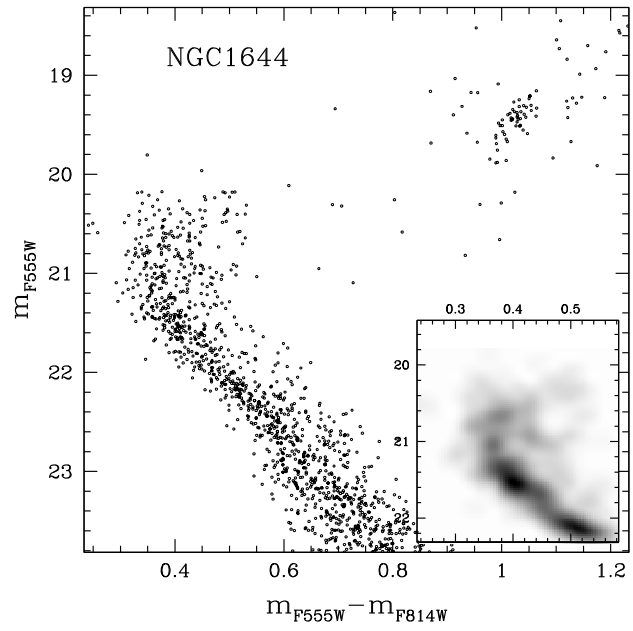


**Fig. 20.** As in Fig. 7 for NGC 1644.

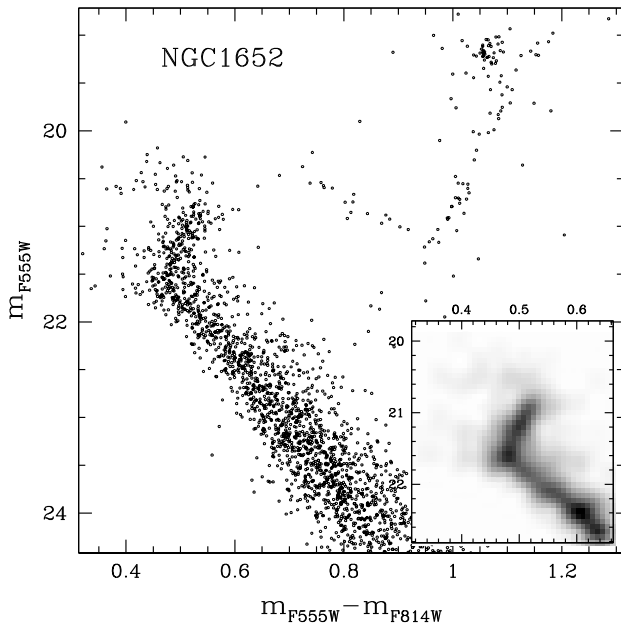


**Fig. 21.** As in Fig. 7 for NGC 1652.

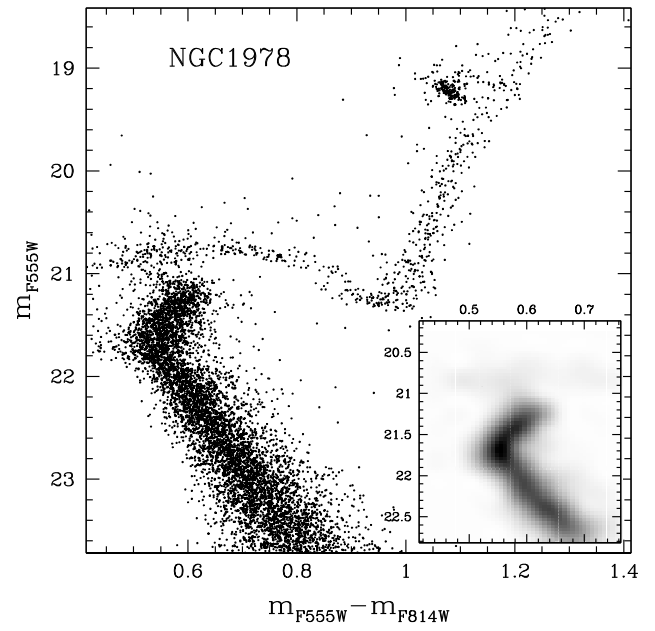


**Fig. 23.** As in Fig. 7 for NGC 1978.

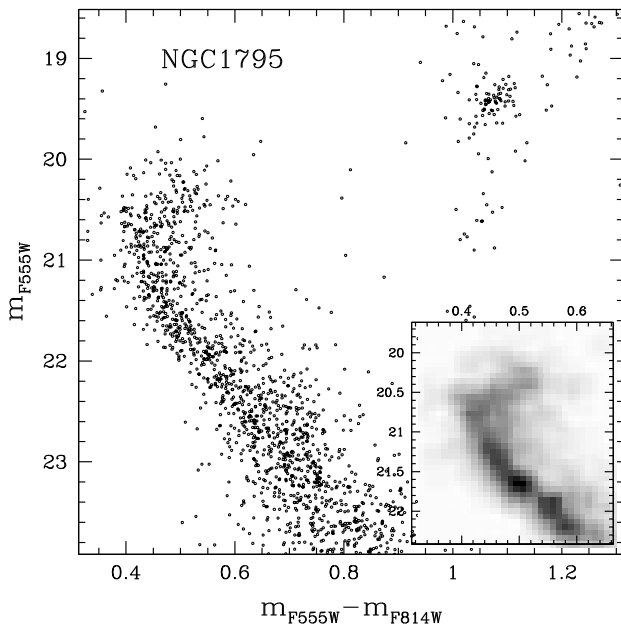


**Fig. 22.** As in Fig. 7 for NGC 1795.

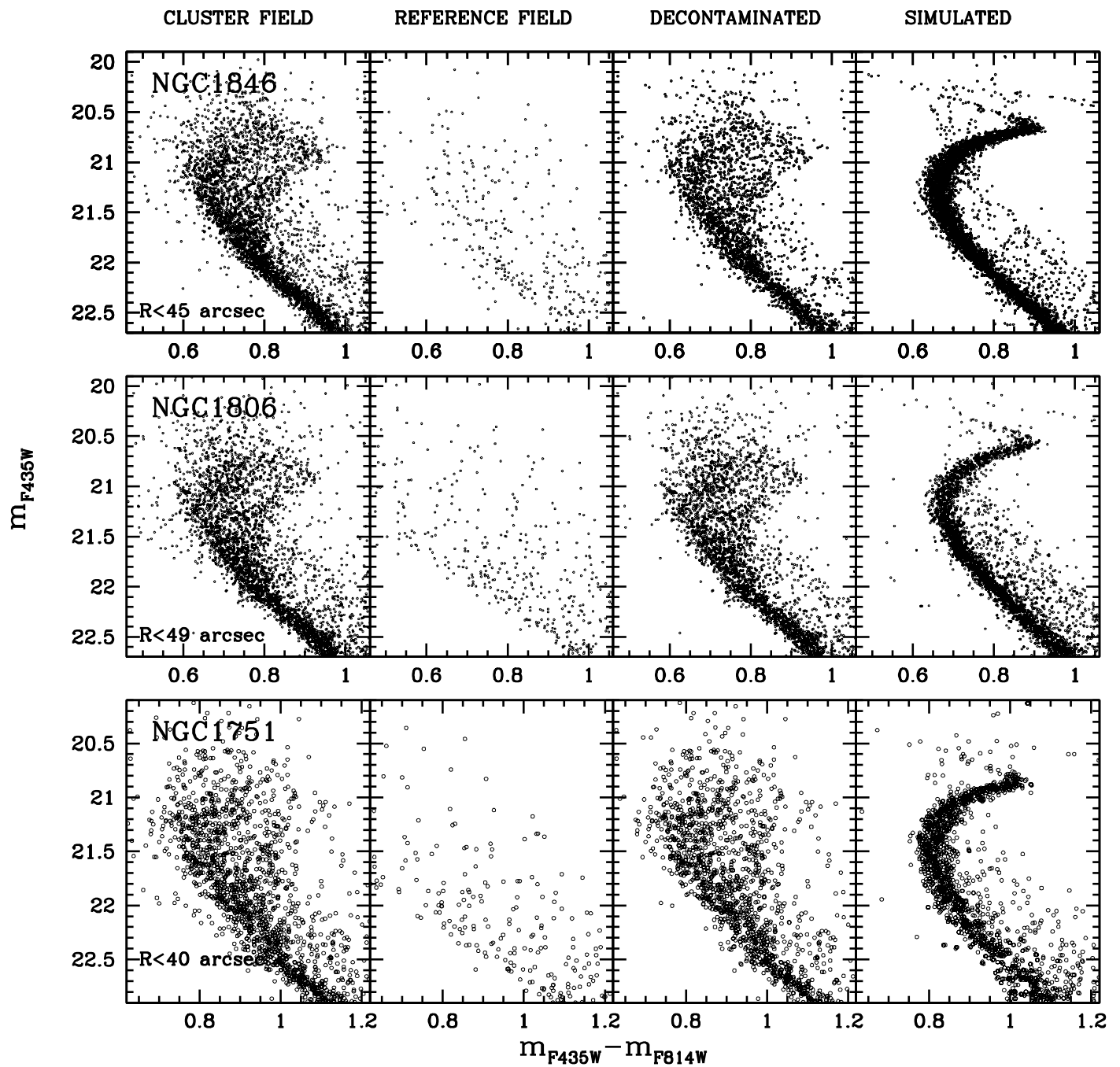


Fig. 32. As in Fig. 31 for NGC 1846, NGC 1806, and NGC 1751.

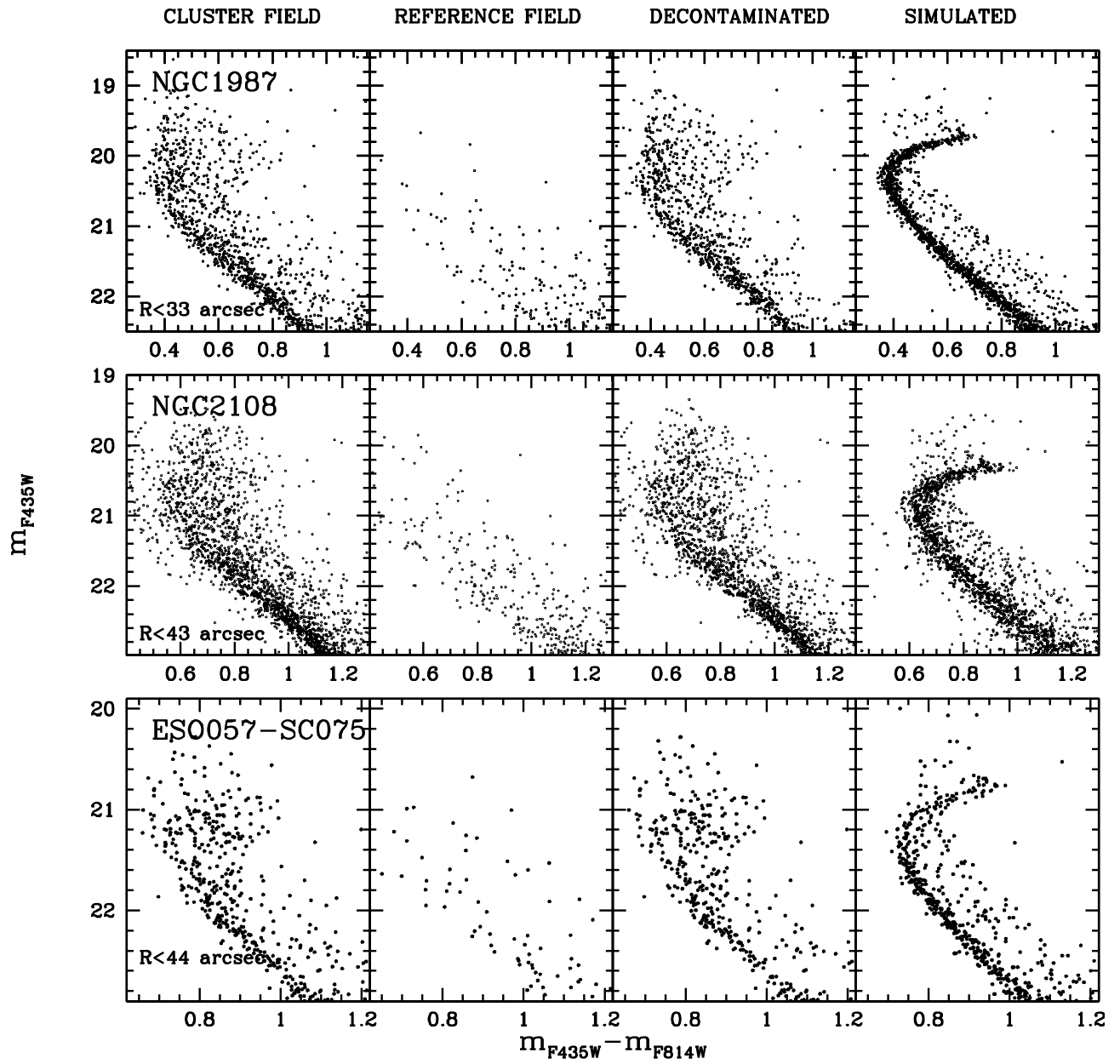


Fig. 33. As in Fig. 31 for NGC 1987, NGC 2108 and ESO057-SC075.

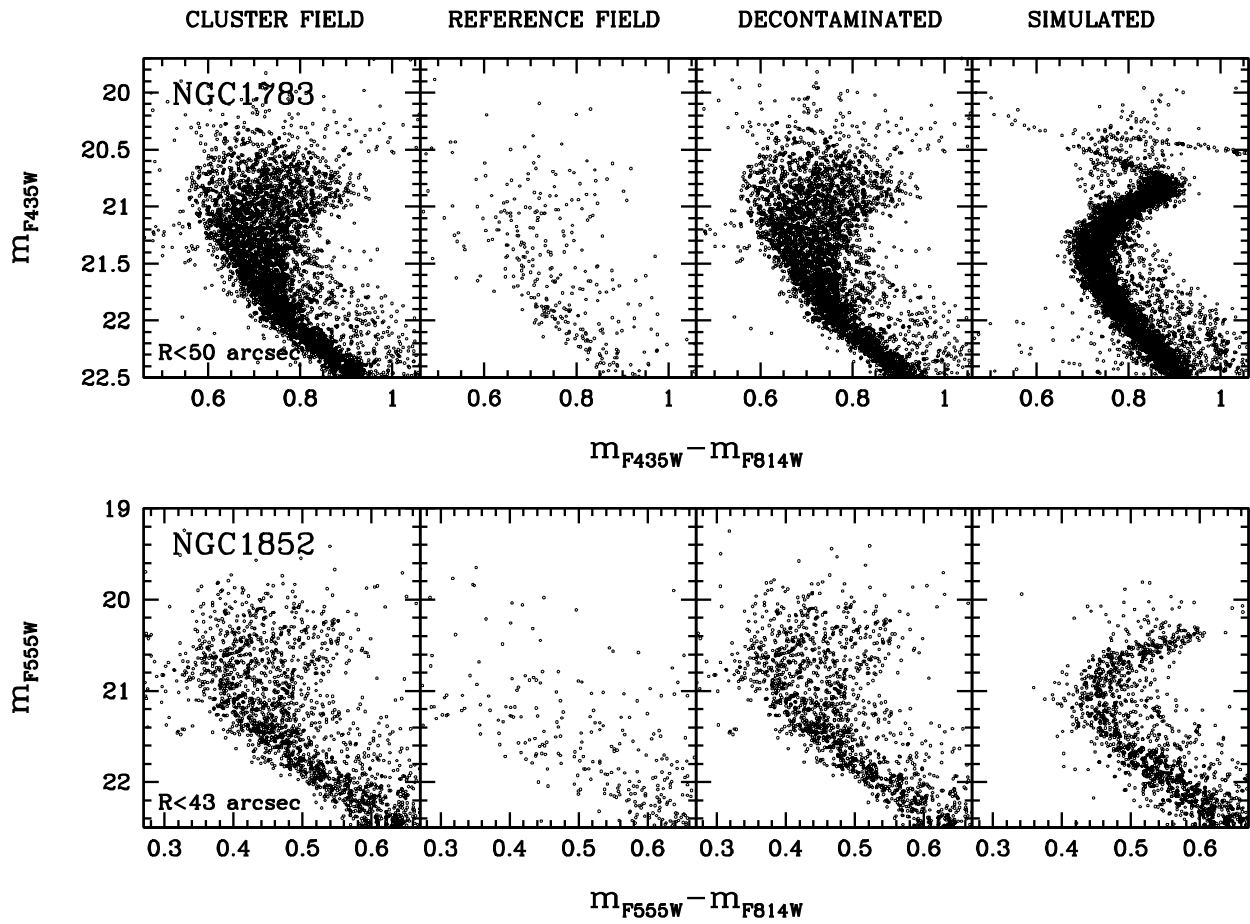


Fig. 34. As in Fig. 31 for NGC 1783 and NGC 1852.

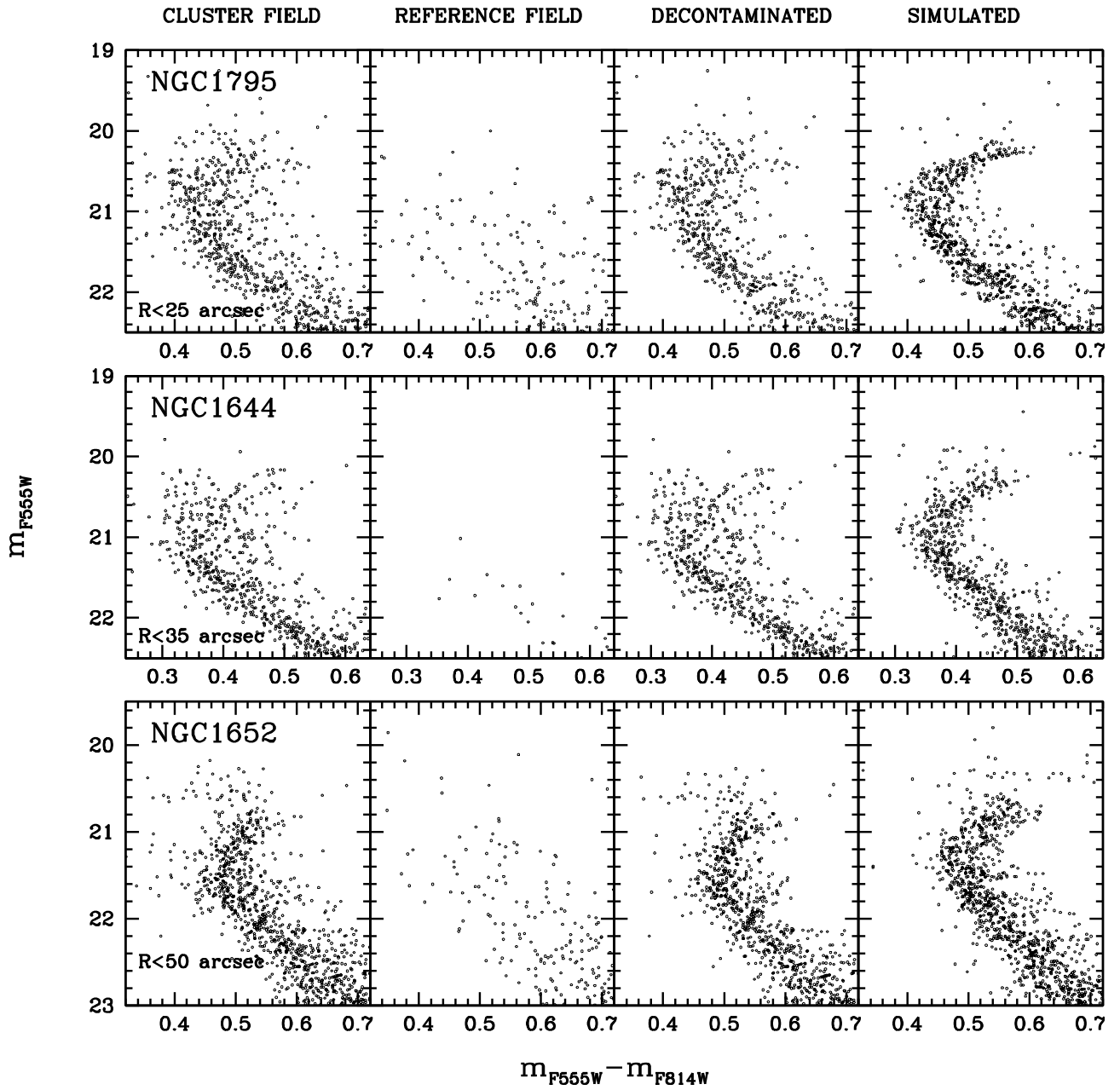


Fig. 35. As in Fig. 31 for NGC 1975, NGC 1644, and NGC 1652.

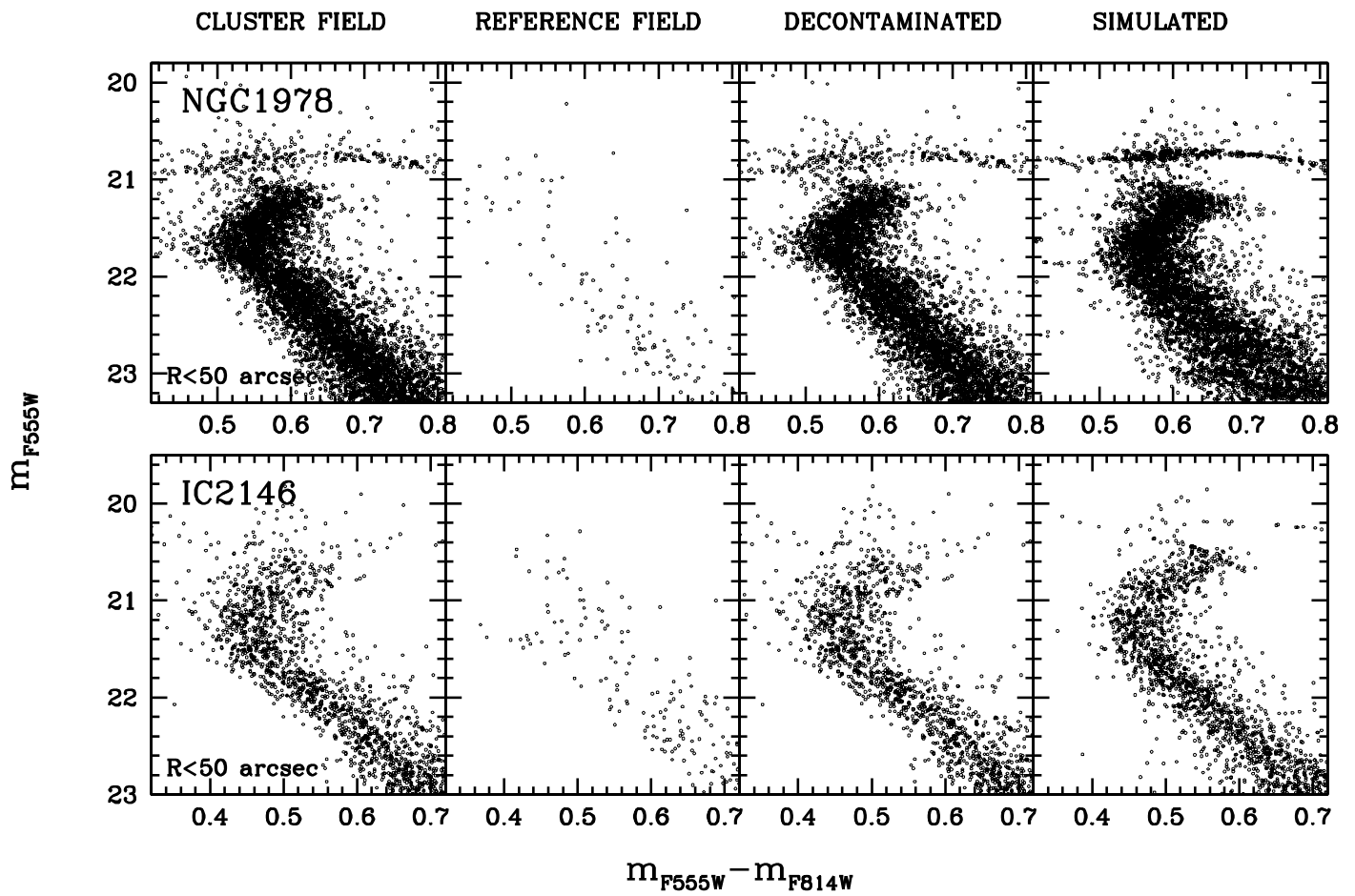


Fig. 36. As in Fig. 31 for NGC 1978 and IC 2146.

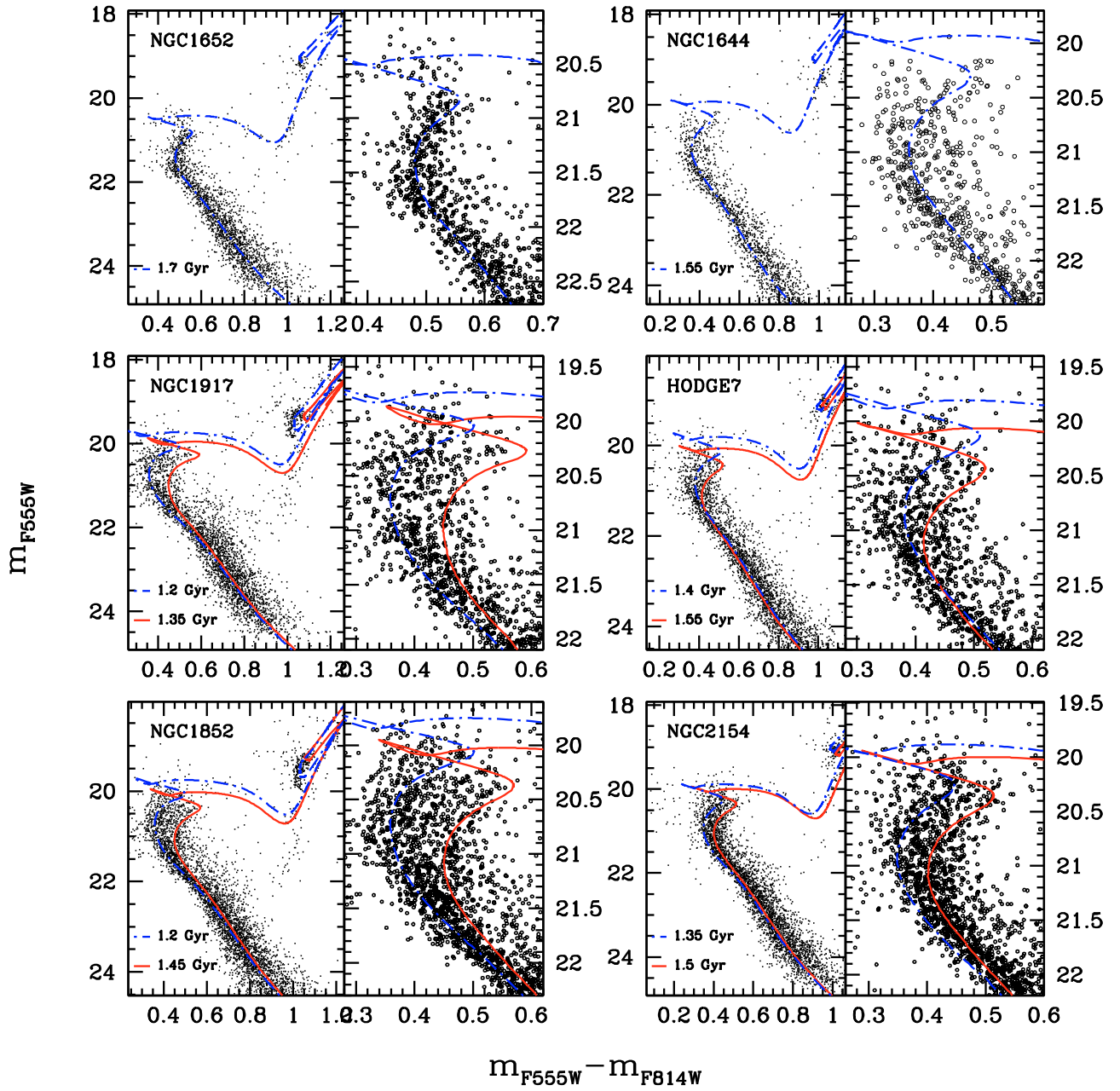


Fig. 38. As in Fig. 37 for NGC 1652, NGC 1644, NGC 1917, HODGE7, NGC 1852, and NGC 2154.

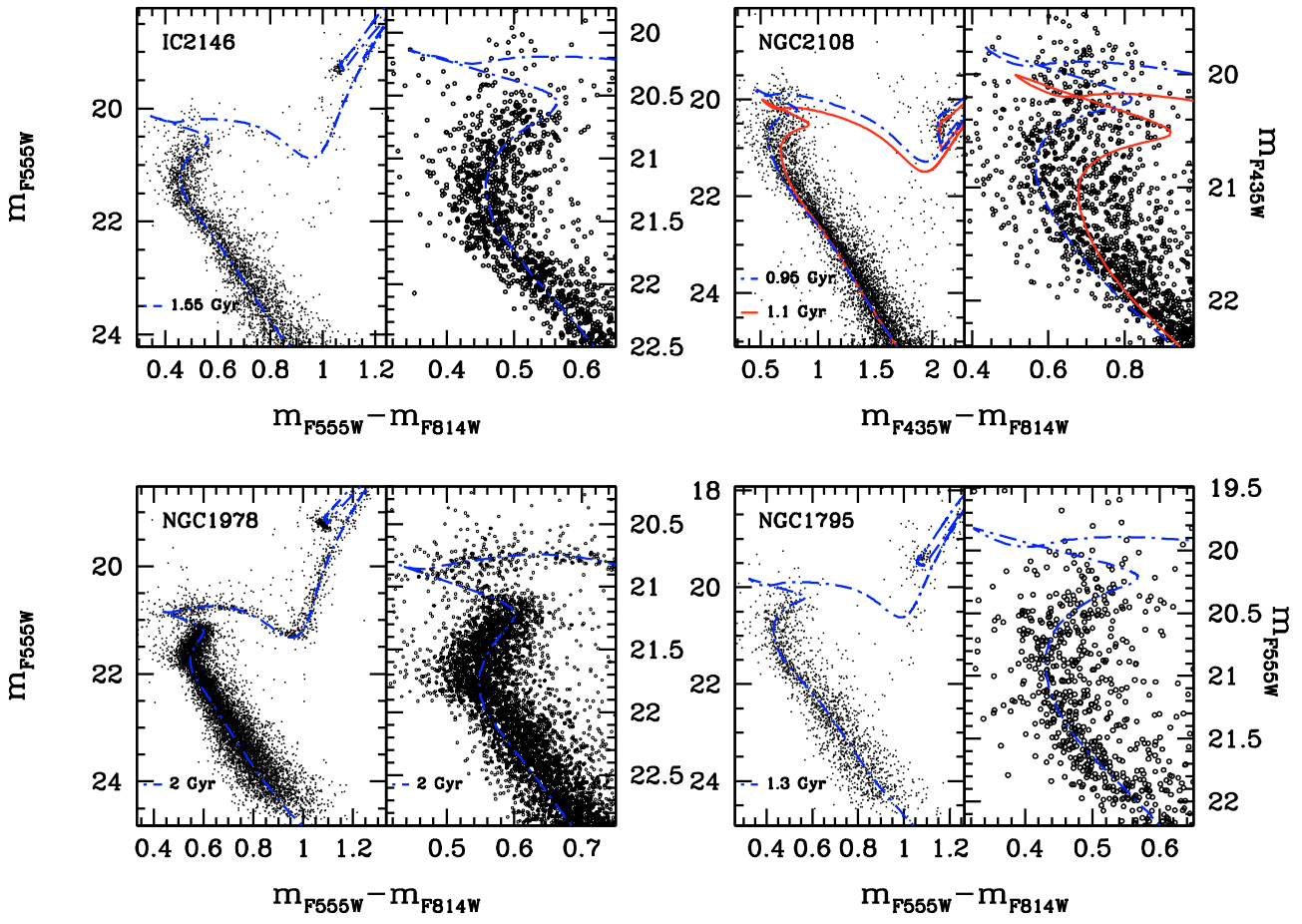


Fig. 39. As in Fig. 37 for IC 2146, NGC 2108, NGC 1978, and NGC 1795.